

AI-Bind: Improving Binding Predictions for Novel Protein Targets and Ligands

Ayan Chatterjee^{1,2,+}, Omair Shafi Ahmed^{3,+}, Robin Walters^{3,+},
Zohair Shafi^{3,+}, Deisy Gysi^{1,4}, Rose Yu⁵, Tina Eliassi-Rad^{2,3},
Albert-László Barabási^{1,4,6}, Giulia Menichetti^{1,4†}

¹Center for Complex Network Research, Northeastern University, Boston, USA

²Network Science Institute, Northeastern University, Boston, USA

³Khoury College of Computer Sciences, Northeastern University, Boston, USA

⁴Department of Medicine, Brigham and Women's Hospital, Harvard Medical School, Boston, USA

⁵Department of Computer Science and Engineering, University of California, San Diego, USA

⁶Center for Network Science, Central European University, Budapest, Hungary

⁺these authors contributed equally to this work

1 ABSTRACT

Identifying novel drug-target interactions (DTI) is a critical and rate limiting step in drug discovery. While deep learning models have been proposed to accelerate the identification process, we show that state-of-the-art models fail to generalize to novel (i.e., never-before-seen) structures. We first unveil the mechanisms responsible for this shortcoming, demonstrating how models rely on shortcuts that leverage the topology of the protein-ligand bipartite network, rather than learning the node features. Then, we introduce AI-Bind, a pipeline that combines network-based sampling strategies with unsupervised pre-training, allowing us to limit the annotation imbalance and improve binding predictions for novel proteins and ligands. We illustrate the value of AI-Bind by predicting drugs and natural compounds with binding affinity to SARS-CoV-2 viral proteins and the associated human proteins. We also validate these predictions via auto-docking simulations and comparison with recent experimental evidence. Overall, AI-Bind offers a powerful high-throughput approach to identify drug-target combinations, with the potential of becoming a powerful tool in drug discovery.

[†]Corresponding author. e-mail: menicgiulia@gmail.com

2 INTRODUCTION

The accurate prediction of drug-target interactions (DTI) is a critical step in drug discovery, helping with the development of new drugs, the discovery of new targets, and reducing the failure rate in clinical trials, when drugs are tested for safety [1–3]. While molecular dynamics simulations [4, 5] are frequently employed to identify potential protein-ligand binding, the computational complexity (namely, run-times) of the simulations and the lack of 3D protein structures significantly limit large-scale testing. Therefore, machine learning (ML) and artificial intelligence (AI) based models have been proposed to circumvent the computational limitations of the existing approaches [6, 7], leading to the development of models that rely either on novel deep learning architectures or innovative chemical feature representations [8–14].

The binding information used for training is extracted from protein-ligand binding databases like DrugBank [15], BindingDB [16], Tox21 [17], ChEMBL [18], Davis [19], or Drug Target Commons [20]. A bipartite network represents the binding information as a graph with two different types of *nodes*: one corresponding to proteins (also called a target, representing for example a human or a viral protein) and the other corresponding to ligands (representing potential drugs or natural compounds), respectively. A protein-ligand annotation, i.e., evidence that a ligand binds to a protein, is represented as a *link* between the protein and the ligand in the bipartite network [21]. Experimentally validated annotations define a drug-target interaction (DTI) network. While binding depends only on the chemical characteristics of the nodes (proteins and ligands), we show that in current ML models predictions are primarily driven by the topology of the DTI network. We begin by analyzing existing training data, i.e., DTI networks derived from databases like BindingDB and DrugBank. We find that the number of annotations linked to a protein or a ligand follows a fat-tailed distribution [22], indicating that the vast majority of proteins and ligands have only a small number of annotations. These proteins and ligands coexist with a few *hubs*, nodes with an exceptionally large number of binding records [21]. For example, the number of annotations for proteins follows a power law distribution with degree exponent $\gamma_p = 2.84$ in the BindingDB data used for training DeepPurpose [8]. The ligands have a degree exponent $\gamma_l = 2.94$ (Figure 1A) [23]. For these degree exponents, the second moment of the distribution diverges for large sample sizes, implying that the expected uncertainty in the binding information characterizing the average number of annotations in the database is highly significant, limiting our ability to predict the binding between a single protein and ligand [21, 24].

Common deep learning frameworks formulate the binding prediction problem as a binary classification task. The successful training of a binary classifier requires pairs of proteins and

ligands that are known to bind to each other, as well as negative samples, i.e., pairs that do not interact or only weakly interact. Such positive and negative annotations are usually determined by thresholding kinetic constants like K_d , which quantifies the propensity of a protein-ligand pair to disassociate into its constituent protein and ligand. However, K_d is not randomly distributed across the records, but the number of annotations k per node and the average K_d across its links (i.e., $\langle K_d \rangle$) are anti-correlated, indicating stronger binding propensity for proteins and ligands with more annotations ($r_{Spearman}(k_p, \langle K_d \rangle) = -0.47$ for proteins, $r_{Spearman}(k_l, \langle K_d \rangle) = -0.29$ for ligands in the BindingDB training data used by DeepPurpose). As the annotations follow fat-tailed distributions, the observed anti-correlation drives the hub proteins and ligands to have disproportionately more binding records on average, whereas proteins and ligands with fewer annotations have more non-binding examples. This *annotation imbalance* prompts the ML models to learn and predict that some proteins and ligands bind disproportionately more often than the others. In other words, the ML models learn the binding patterns from the degree of the nodes, neglecting relevant node features, like the chemical structures of the ligands or the amino-acid sequences of the proteins [8, 25–27]. This annotation imbalance offers good performance as quantified by the Area Under the Receiver Operating Characteristics (AUROC) and the Area Under the Precision Recall Curve (AUPRC) for the unknown annotations associated with the missing links in the protein-ligand interaction network used for training, a phenomenon we term the *emergence of topological shortcuts* (see Section S1). A key consequence and a signal of such topological shortcuts is the degradation of the performance of an ML model when asked to predict binding between novel (i.e., never-before-seen) protein targets and ligands. The loss of performance is particularly significant for natural compounds as ligands, which have less binding information in the training data, and have more complex structures compared to drugs (see Section S2). This modeling limitation is in-line with the findings of Geirhos et al. [28], who showed that deep learning methods tend to exploit shortcuts in training data to achieve good performance. Lee et al. [29] and Wang et al. [30] proposed approaches that partly address shortcut learning, but fail to generalize to unexplored proteins, i.e., proteins that lack sufficient binding annotations, or originate from organisms with no close relatives in current protein databases.

Here, we propose AI-Bind, a pipeline for predicting protein-ligand binding which can successfully generalize to unseen proteins and ligands. AI-Bind combines network science methods with unsupervised pre-training to control for the over-fitting and the annotation imbalance of existing libraries. We leverage the notion of shortest path distance on a network to identify distant protein-ligand pairs as negative samples. Combining these network-derived negatives

with experimentally validated non-binding protein-ligand pairs, we ensure sufficient positive and negative samples for each node in the training data. Additionally, AI-Bind learns, in an unsupervised fashion, the representation of the node features, i.e., the chemical structures of ligand molecules or the amino-acid sequences of protein targets, helping circumvent the model’s dependency on limited binding data. Instead of training the deep neural networks in an end-to-end fashion using binding data, we pre-train the embeddings for ligands and proteins using larger chemical libraries, allowing us to generalize the prediction task to chemical structures, beyond those present in the training data.

3 RESULTS

Limitations of existing ML models

ML models characterize each node (proteins and ligands) and its likelihood to bind to other nodes according to the features and annotations in the training data. While annotations capture known protein-ligand interactions, features refer to the chemical structures of proteins and ligands which determine their physical and chemical properties, and are expressed as amino acid sequences or 3D structures for proteins, and chemical SMILES [31] for ligands. In an ideal scenario, the ML model learns the patterns characterizing the features which drive the protein-ligand interactions, as it is the physical and chemical properties of a protein and of a ligand that determine the binding affinity between them. Yet, as we show next, the existing ML models ignore the features and rely largely on annotations, i.e., the degree information for each protein and ligand in the DTI network, as a shortcut to make new binding predictions. For each node i with number of annotations k_i , we quantify the balance of the available training information via the *degree ratio*,

$$\rho_i = \frac{k_i^+}{k_i^+ + k_i^-} = \frac{k_i^+}{k_i}, \quad (1)$$

where, k_i^+ is the positive degree, corresponding to the number of known binding annotations in the training data, and k_i^- is the negative degree, or the number of known non-binding annotations in the training data (Figure 1C). As the training data lacks either binding or non-binding annotations for most proteins and ligands (Table 1), the resulting $\{\rho_i\}$ are close to 1 or 0 (Figs. 2A, B). Proteins (and ligands) with significantly more binding annotations compared to the non-binding ones have $\rho \rightarrow 1$, and those with more non-binding annotations compared to the binding annotations have $\rho \rightarrow 0$. These extreme ρ values represent the annotation imbalance in the prediction problem.

The annotation imbalance is a major source of false positives (Figs. 2A, B) and false

negatives (see Section S3). As many state-of-the-art deep learning models, such as DeepPurpose [8], uniformly sample the available positive and negative annotations, they assign higher binding probability to proteins and ligands with higher ρ . Consequently, their binding predictions are driven by topological shortcuts in the protein-ligand network, which are associated with the the positive and negative annotations present in the training data rather than the features characterizing proteins and ligands, such as the molecular fingerprint of a ligand or the amino-acid sequence of a protein.

The higher binding probabilities in DeepPurpose for proteins and ligands with large degree ratios (Figs. 2D, E) prompted us to compare the performance of DeepPurpose with network configuration models, algorithms that ignore the features of proteins and ligands and instead predict the likelihood of binding by leveraging only topological constraints derived from the network degree sequence [21, 32–34]. In the configuration model (Figure 3A, Methods), the probability of observing an absent link is determined only by the the degrees of its end nodes. In a 5-fold cross-validation on the benchmark BindingDB dataset (Table 1), we find the top-performing DeepPurpose architecture, Transformer-CNN [8], achieves an overall AUROC of $0.85 (\pm 0.005)$ and AUPRC of $0.65 (\pm 0.008)$. At the same time, the network configuration model on the same data achieves an AUROC of $0.86 (\pm 0.005)$ and AUPRC of $0.61 (\pm 0.008)$ (Figure 3B). Hence, the network configuration model, relying only on annotations, performs just as well as the deep learning model, confirming that the topology of the protein-ligand network drives the predictive power of the ML model. To further investigate this hypothesis, we tested three distinct scenarios: (i) unseen edges (Transductive test), when both proteins and ligands from the test dataset are present in the training data; (ii) unseen targets (Semi-inductive test), when only the ligands from the test dataset are present in the training data; (iii) unseen nodes (Inductive test), when both proteins and ligands from the test dataset are absent in the training data.

We find that both DeepPurpose and the configuration model perform well in scenarios (i) and (ii) (Figures 3C, D). However, for the inductive test scenario (iii), when confronted with new proteins and ligands, both performances drop significantly (Table 2). DeepPurpose has an AUROC of $0.60 (\pm 0.066)$ and AUPRC of $0.42 (\pm 0.063)$, comparable to the configuration model, for which we have AUROC of 0.50 and AUPRC of $0.30 (\pm 0.034)$. To offer a final piece of evidence that DeepPurpose disregards node features, we randomly shuffled each fingerprint and amino acid sequence in the training set, while keeping the same positive and negative annotations per node. We did not observe a substantial drop in the test performance (Table 3). These tests confirm that DeepPurpose leverages network topology as a learning shortcut and

fails to generalize predictions to proteins and ligands beyond the training data, indicating that we must use inductive testing to evaluate the true performance of ML models.

AI-Bind and statistics across models

AI-Bind is a deep learning pipeline that combines network-derived learning strategies with unsupervised pre-trained node features, to optimize the exploration of the binding properties of novel proteins and ligands. Our pipeline is compatible with various neural architectures, three of which we propose in the paper: VecNet, Siamese model, and VAENet. AI-Bind uses two inputs (Figure 4A): First, for ligands, AI-Bind takes as input isomeric SMILES [31], which capture structures of ligand molecules. AI-Bind considers a search-space consisting of all the drug molecules available in DrugBank and the naturally occurring compounds in Natural Compounds in Food Database (NCFD) (see Section S4.4), and can be extended by leveraging larger chemical libraries like PubChem [35]. Second, for proteins, AI-Bind uses as input the amino acid sequences retrieved from the protein databases Protein Data Bank (PDB) [36], the Universal Protein knowledgebase (UniProt) [37], and GeneCards [38].

AI-Bind benefits from several novel features compared to the state-of-the-art: (a) It relies on network-derived negatives to balance the number of positive and negative samples for each protein and ligand. To be specific, it uses protein-ligand pairs with shortest path distance ≥ 7 as negative samples, ensuring that the neural networks observe both binding and non-binding examples for each protein and ligand (see Figure 5, Methods, Section S5). (b) During unsupervised pre-training, AI-Bind trains the node embeddings on larger collections of chemical and protein structures, compared to the set with known binding annotations, allowing AI-Bind to learn a wider variety of structural patterns. Indeed, while models like DeepPurpose were trained on 862,337 ligands and 7,504 proteins provided in BindingDB, or 7,307 ligands and 4,762 proteins provided in DrugBank, the unsupervised representation in AI-Bind’s VecNet is trained on 19.9 million compounds [39] and 546,790 proteins [40].

We begin the model’s validation by systematically comparing the performance of AI-Bind to DeepPurpose and the configuration model on a 5-fold cross-validation using the network-derived dataset for transductive, semi-inductive, and inductive tests (Figs. 4C, E, F). We find that the configuration model performs poorly in inductive testing (AUROC 0.5, AUPRC 0.469 ± 0.014). Due to the network-derived negatives removing the annotation imbalance, DeepPurpose shows improved performance for novel proteins and ligands (AUROC 0.642 ± 0.025 , AUPRC 0.583 ± 0.016). The best performance on unseen nodes is observed for AI-Bind’s VecNet, with AUROC of 0.745 ± 0.032 and AUPRC of 0.729 ± 0.038 (see Table S3). The model

uses pre-trained `mol2vec` [39] and `protvec` [40] embeddings combined with a simple multi-layer perceptron [41] to learn protein-ligand binding (Figure 4B, see Methods). In particular, the unsupervised pre-training for ligand embeddings allows us to generalize AI-Bind to naturally occurring compounds, characterized by complex chemical structures and fewer training annotations compared to drugs (see section S2), obtaining performances comparable to that obtained for drugs (Figure 4D).

Binding validation on COVID-19 proteins

For a better understanding of the reliability of the AI-Bind predictions, we move beyond standard ML cross-validation and compare our predictions with molecular dynamics simulations and in vitro and clinical results on protein-ligand binding. Auto-docking simulations offer a reliable but computationally complex method to predict (or validate) binding between proteins and ligands [42]. Motivated by the need to model rapid response to sudden health crises, we chose as our validation set the 26 SARS-CoV-2 viral proteins and the 332 human proteins targeted by SARS-CoV-2 viral proteins [43, 44]. These proteins are missing from the training data of AI-Bind, hence represent novel targets and allow us to rely on recent studies on COVID-19 to validate the AI-Bind predictions. We obtain the amino acid sequences for 16 SARS-CoV-2 viral proteins and 330 human proteins from UniProt [37], and use them as input to AI-Bind’s VecNet. Binding between viral and human proteins is necessary for the virus to synthesize its own viral proteins and to facilitate its replication. Our goal is to predict drugs in DrugBank or naturally occurring compounds that can bind to the 346 proteins associated with COVID-19, potentially disrupting the viral infection. After sorting all protein-ligand pairs based on their binding probability predicted by AI-Bind’s VecNet (p_{ij}^{VecNet}), we tested the top 100 and bottom 100 with blind auto-docking simulations using AutoDock Vina [42], which estimates binding affinity by considering all possible binding locations on the 3D protein structures. Of the 54 proteins present in the top 100 and bottom 100 predicted pairs, 23 had 3D structures available in PDB [36], and 51 of 59 listed ligand structures were available on PubChem [35], allowing us to perform 128 auto-docking simulations (84 for the top and 44 for the bottom predictions). We find that the median binding affinity for the top VecNet predictions is -7.65 kcal/mole, while for the bottom ones we find -3.0 kcal/mole (Figure 6A), confirming that for AI-Bind, the top predictions show considerably higher binding propensity than the bottom ones. As a second test, we obtained the binary labels (binding or non-binding) from auto-docking and AI-Bind predictions using the threshold of -1.75 kcal/mole on the binding affinities [45] and the optimal threshold on p_{ij}^{VecNet} corresponding to the highest F1-Score on the inductive test set (see Section

S7, Figure S11). We construct the confusion matrix with these labels, observing F1-Score = 0.82 for the AI-Bind predictions, an excellent value confirming that the rank list provided by AI-Bind predictions shows a significant similarity to the rank list obtained by binding affinities compared to a random selection (Figure 6B). We further check the stability of these performance metrics by randomly choosing 20 protein-ligand pairs in a 5-fold bootstrapping set-up and observe that F1-Score = 0.90 ± 0.02 . Additionally, we find that the predictions made by AI-Bind’s VecNet (p_{ij}^{VecNet}) and the free energy of protein-ligand binding obtained from auto-docking (ΔG) are anti-correlated with $r_{Spearman}(p_{ij}^{VecNet}, \Delta G) = -0.51$. The top 20 VecNet predictions show $r_{Spearman}(p_{ij}^{VecNet}, \Delta G) = -0.17$. As lower binding affinity values corresponds to stronger binding, these results document the agreement between AI-Bind predictions and auto-docking simulations.

Among the 50 ligands with the highest average binding probability we find two FDA-approved drugs Anidulafungin (NDA#021948) and Cyclosporine (ANDA#065017). Experimental evidence [46] shows that these drugs have anti-viral activity at very low concentrations in the dose-response curves, and have IC_{50} values of $4.64 \mu M$ and $5.82 \mu M$, respectively (Figure 6C), measured by immunofluorescence analysis with an antibody specific for the viral N protein of SARS-CoV-2. These low IC_{50} values support anti-viral activity, confirming that Anidulafungin and Cyclosporine bind to COVID-19 related proteins, and the activity at low concentrations indicate that they are safe to use for treating COVID-19 patients. Anidulafungin binds to the SARS-CoV-2 viral protein nsp12, a key therapeutic target for coronaviruses [47].

AI-Bind also offers several novel predictions with potential therapeutic relevance. For example, it predicts that the naturally occurring compounds Spironolactone, Oleanolic acid, and Echinocystic acid are potential ligands for COVID-19 proteins, all three ligands binding to Tripartite motif-containing protein 59 (TRIM59), a human protein to which the SARS-CoV-2 viral proteins ORF3a and NSP9 bind [48, 49]. AutoDock Vina supports these predictions, offering binding affinities -7.1 kcal/mole, -8.0 kcal/mole, and -7.6 kcal/mole, respectively.

Spironolactone, found in rainbow trout [50], has multiple known therapeutic effects, including preventing pulmonary fibrosis, a major long-term complication of COVID-19 [51, 52]. Oleanolic acid is present in apple, tomato, strawberry, and peach, and has been proposed as a potential anti-viral agent for COVID-19 [53, 54]. Oleanolic acid, which passed the drug efficacy benchmark ADME (Absorption, Distribution, Metabolism, and Excretion), plays an important role in controlling viral replication of SARS-CoV-2 [55] and is effective in preventing virus entry at low viral loads [54]. Finally, Echinocystic acid, found in sunflower, basil, and gala apples, is known for its anti-inflammatory [56–58] and anti-viral activity [59, 60], but its potential

anti-viral role in COVID-19 is yet to be validated.

In summary, ML models often fail in real world settings when making predictions on data that they were not explicitly trained upon despite achieving good test performance based on traditional ML-based metrics [61]. It is therefore necessary to validate the applicability of these models before deploying them. The documented validation of the AI-Bind predictions with molecular dynamic simulations and in vitro experiments offers us confidence AI-Bind is an effective prioritization tool in diverse settings.

4 DISCUSSION

The accurate prediction of drug-target interactions is an essential precondition of drug discovery. Here we showed that by taking topological shortcuts, existing deep learning models significantly limit their predictive power. Indeed, a mechanistic and quantitative understanding of the origins of these shortcuts indicates that uniform sampling in the presence of annotation imbalance drives ML models to disregard the features of proteins and ligands, limiting their ability to generalize to novel protein targets and ligand structures. To address these shortcomings, we introduced a new pipeline, AI-bind, which mitigates the annotation imbalance of the training data by introducing network-derived negative annotations inferred via shortest path distance and improves the transferability of the ML models to novel protein and ligand structures by unsupervised pre-training. The proposed unsupervised pre-training of node features also influences the quality of false predictions, removing potential structural biases towards specific protein families (see Section S8). Once we improved the statistical sampling of the training data and generated the node embeddings in an unsupervised fashion, we observed an increase in performance compared to DeepPurpose, resulting in commendable AUROC (24% improvement) and AUPRC (74% improvement) and, most importantly, an ability to predict beyond proteins and ligands present in the training dataset.

A major limitation of using binding predictions in drug discovery is that binding to disease-related protein targets does not always imply a therapeutic treatment. As future work, we plan to extend our implementation by introducing an ML-based classifier to sort the list of potential ligands according to their pharmaceutical (therapeutic) effects, combining the current node features with additional metrics derived from traditional network medicine approaches [62, 63].

AI-Bind leverages ligands' Morgan fingerprints and proteins' amino acid sequences, which encode relevant properties of the molecules: from the presence of hydrogen donors, hydrogen acceptors, count of different atoms, chirality, and solubility for ligands, to the existence of R groups, N or C terminus in proteins. All these properties influence the mechanisms driving

protein-ligand binding (see Section S9) [64]. Yet, the binding phenomenon is largely dependent on the 3D structures of the molecules, which determines the binding pocket structures and the rotation of the bonds. We plan to embed the 3D structures of protein and ligand molecules, which will take into account higher order molecular properties driving protein-ligand binding and refine the predictive power of AI-Bind. To maximize generalization across 3D structure, we will use SE(3) equivariant networks to learn embeddings. Equivariance has proven to be a powerful tool for improving generalization over molecular structure [65–67]. We also plan to explore the performance of AI-Bind over the entire druggable genome [68], allowing us to predict for each protein, which domains are responsible for the binding predictions, revealing binding locations of the ligands and the proteins. Finally, we envision enabling AI-Bind to predict the kinetic constants K_d , K_i , IC_{50} , and EC_{50} by formulating a regression task over these variables.

The existing auto-docking infrastructures allow screening for a specific protein structure against wide chemical libraries. Indeed, VirtualFlow [69], an open-source drug discovery platform offers virtual screening over more than 1.4 billion commercially available ligands. However, running docking simulations over these vast libraries incurs high costs for data preparation and computation time and are often limited to only proteins with 3D structures [36]. For example, in our validation step, only half (23 out of 54) of the 3D structures of the proteins associated with COVID-19 were available. Since AI-Bind only requires the chemical SMILES for ligands [31] and amino acid sequences for proteins, it can offer fast screening for large libraries of targets and molecules without requiring 3D structures, guiding the computationally expensive auto-docking simulations on selected protein-ligand pairs.

5 METHODS

Data Preparation

We use InChIKeys [70] and amino acid sequences as the unique identifiers for ligands and targets, respectively. Positive and negative samples are selected from DrugBank, BindingDB and DTC (see Section S4). We consider samples from BindingDB and DTC to be binding or non-binding based on the kinetic constants K_i , K_d , IC_{50} , and EC_{50} . We use thresholds of $\leq 10^3 nM$ and $\geq 10^6 nM$ to obtain positive and (absolute) negative annotations, respectively [45]. We then filter out all samples outside the temperature range 20°C-45°C to remove ambiguous pairs. All amino acid sequences were obtained from UniProt [37].

Positive Samples

We consider the binding information from DrugBank as positive samples. From these annotations, we removed 53 pairs which are available in BindingDB and have kinetic constants $\geq 10^6 nM$. To obtain additional positive samples for drugs, we searched in BindingDB using their InChIKeys. We obtained 4,330 binding annotations from BindingDB related to the drugs in DrugBank. Overall, we gathered a total of 28,188 positive samples for drugs. We identified naturally occurring/food-borne compounds by leveraging the Natural Compounds in Food Database (NCFD) database (see Section S4.4). We queried BindingDB and DTC with the associated InChIKeys, obtaining a total of 1,555 positive samples.

Network-Derived Negative Samples

To generate annotation-balanced training data for AI-Bind, we merged the positive annotations derived from DrugBank, BindingDB, and DTC, for a total of 5,104 targets and 8,111 ligands, of which 485 are naturally occurring, and calculated the shortest path distribution. All odd-path lengths in the bipartite network correspond to protein-ligand pairs (Figure 5C). Overall, the longer the shortest path distance separating a protein and a ligand, the higher the kinetic constant observed in BindingDB (Figure 5D). In particular, pairs more than 7 hops apart have, on average, kinetic constants $K_i \geq 10^6 nM$, which is generally considered above the protein-ligand binding threshold [45] (see Section S5). We randomly selected a subset of protein-ligand pairs which are 7 hops apart as negative samples, to create an overall class balance between positive and negative samples in the training data. Finally, we removed all nodes with only positive or only negative samples and obtained the *network-derived negative samples*. We performed testing and validation on ≥ 11 -hop distant pairs. Additionally, we included in testing and validation the absolute non-binding pairs derived from BindingDB by thresholding the kinetic constants (K_i , K_d , IC_{50} , and EC_{50}).

Network Configuration Model

Overview

Protein-ligand annotations are naturally embedded in a bipartite duplex network, consisting of a set of nodes, comprising all proteins and ligands, interacting in two layers, each reflecting a distinct type of interaction linking the same pair of nodes [33]. More specifically, one layer (Layer 1) captures the positive or binding annotations, while the second layer (Layer 2) collects the negative or non-binding annotations (Figure 3A). A multilink \mathbf{m} between two nodes encodes the

pattern of links connecting these nodes in different layers. In particular, $\mathbf{m} = (1, 0)$ indicates positive interactions, $\mathbf{m} = (0, 1)$ refers to negative interactions, $\mathbf{m} = (0, 0)$ represents the absence of any type of annotations, and $\mathbf{m} = (1, 1)$ is mathematically forbidden, as binding and non-binding cannot coexist for the same pair of protein and ligand.

We developed a canonical bipartite duplex null model that conserves on average the number of positive and negative annotations of each node, while correctly rewiring positive and negative links and avoiding forbidden configurations. By means of entropy maximization with constraints, we derive the analytical formulation of each multilink probability and the conditional probability of observing positive binding once an annotation is reported.

Mathematical Formulation

Let $A_{ij}^{\mathbf{m}}$ be the multi-adjacency matrix representing the bipartite duplex of ligands ($\{i\}$) and proteins ($\{j\}$), with elements equal to 1 if there is a multilink \mathbf{m} between i and j and zero otherwise. We define the multidegree of ligand i and target j as

$$k_i^{\mathbf{m}} = \sum_{j=1}^{N_T} A_{ij}^{\mathbf{m}}, \quad t_j^{\mathbf{m}} = \sum_{i=1}^{N_L} A_{ij}^{\mathbf{m}}, \quad (2)$$

where N_T is the number of targets and N_L is the number of ligands.

A bipartite duplex network ensemble can be defined as the set of all duplexes satisfying a given set of constraints, such as the expected multidegree sequences defined in Eq. 2. We determine the probability of observing a bipartite duplex network $P(\vec{G})$ by entropy maximization with multidegree constraints $\{k_i^{(1,0)}\}$, $\{k_i^{(0,1)}\}$, $\{t_j^{(1,0)}\}$, and $\{t_j^{(0,1)}\}$, and corresponding Lagrangian multipliers $\{\lambda_i^{(1,0)}\}$, $\{\lambda_i^{(0,1)}\}$, $\{\mu_j^{(1,0)}\}$, and $\{\mu_j^{(0,1)}\}$ [33, 34, 71]. The probability $P(\vec{G})$ factorizes as

$$P(\vec{G}) = \frac{1}{Z} \prod_{ij} \exp \left[- \sum_{\mathbf{m} \neq (0,0), (1,1)} (\lambda_i^{\mathbf{m}} + \mu_j^{\mathbf{m}}) A_{ij}^{\mathbf{m}} \right], \quad (3)$$

with

$$Z = \prod_{ij} \left[1 + \sum_{\mathbf{m} \neq (0,0), (1,1)} e^{-(\lambda_i^{\mathbf{m}} + \mu_j^{\mathbf{m}})} \right]. \quad (4)$$

Multilink probabilities $p_{ij}^{\mathbf{m}}$ are determined by the derivatives of $\log(Z)$ according to $(\lambda_i^{\mathbf{m}} + \mu_j^{\mathbf{m}})$. For instance, the probability of observing a positive annotation is

$$p_{ij}^{(1,0)} = \frac{e^{-(\lambda_i^{(1,0)} + \mu_j^{(1,0)})}}{1 + e^{-(\lambda_i^{(1,0)} + \mu_j^{(1,0)})} + e^{-(\lambda_i^{(0,1)} + \mu_j^{(0,1)})}}, \quad (5)$$

while the probability of observing a negative annotation follows

$$p_{ij}^{(0,1)} = \frac{e^{-(\lambda_i^{(0,1)} + \mu_j^{(0,1)})}}{1 + e^{-(\lambda_i^{(1,0)} + \mu_j^{(1,0)})} + e^{-(\lambda_i^{(0,1)} + \mu_j^{(0,1)})}}, \quad (6)$$

with $p_{ij}^{(1,0)} + p_{ij}^{(0,1)} + p_{ij}^{(0,0)} = 1$.

In this theoretical framework, binding prediction is inherently conditional, as for each ligand i and protein j , we test only the presence of positive and negative annotations. Consequently, $p_{ij}^{(1,0)}$ and $p_{ij}^{(0,1)}$ are normalized by the probability of observing a generic annotation $p_{ij}^{(1,0)} + p_{ij}^{(0,1)}$. In case of unseen edges, binding prediction is determined by

$$p_{ij}^{\text{conditional}} = \frac{p_{ij}^{(1,0)}}{p_{ij}^{(1,0)} + p_{ij}^{(0,1)}}, \quad (7)$$

while in case of unseen target j^* , the binding probability towards a known compound i follows

$$p_{ij^*}^{\text{conditional}} = \frac{\langle p_{ij}^{(1,0)} \rangle_j}{\langle p_{ij}^{(1,0)} \rangle_j + \langle p_{ij}^{(0,1)} \rangle_j} = \rho_i, \quad (8)$$

where $\langle \cdot \rangle_j$ denotes the average over all known targets, and ρ_i follows from Eq. 1.

In case of unseen ligand i^* and target j^* , the binding probability is determined by the overall number of positive ($L^{(1,0)}$) and negative ($L^{(0,1)}$) annotations, i.e.,

$$p_{i^*j^*}^{\text{conditional}} = \frac{\langle p_{ij}^{(1,0)} \rangle_{ij}}{\langle p_{ij}^{(1,0)} \rangle_{ij} + \langle p_{ij}^{(0,1)} \rangle_{ij}} = \frac{L^{(1,0)}}{L^{(1,0)} + L^{(0,1)}}, \quad (9)$$

where $\langle \cdot \rangle_{ij}$ indicates the average over all known pairs of ligands and targets.

Novel Deep Learning Architectures

VecNet

VecNet uses the pre-trained `mol2vec` [39] and `protvec` [40] models (Figure 4B). These models create 300- and 100-dimensional embeddings for ligands and proteins, respectively. Based on `word2vec` [72], they treat the Morgan fingerprint [73] and the amino acid sequences as sentences, where words are fingerprint fragments or amino acid trigrams. The training is unsupervised and independent from the following binding prediction task.

VAENet

VAENet uses a Variational Auto-Encoder [74], an unsupervised learning technique, to embed ligands onto a latent space. The Morgan fingerprint is directly fed to convolutional layers. The auto-encoder creates latent space embeddings by minimizing the loss of information while reconstructing the molecule from the latent representation. We train the Variational Auto-Encoder on 9.5 million chemicals from ZINC database [75], and all drugs and natural compounds in our binding dataset. Similar to VecNet, we use ProtVec for target embeddings.

Siamese Model

The Siamese model embeds ligands and proteins into the same space using a one-shot learning approach [76]. We construct triplets of the form ⟨protein target, non-binding ligand, binding ligand⟩ and train the model to find an embedding space that maximizes the Euclidean distances between non-binding pairs, while minimizing it for the binding ones.

Acknowledgement

We thank Noah DeMoes from Lincoln Laboratory for helping out with setting up the DeepPurpose models. Brennan Klein from Northeastern University has helped us by providing ideas for visualizing the results.

Author Contributions

A.C. contributed to writing the manuscript, data curation and preparation, generating the predictions for the network configuration model, performing experiments to identify the emergence of topological shortcuts, implementing negative sample generation, developing and testing of VecNet and VAENet, and running auto-docking simulations.

O.S.A. contributed to the deep learning literature review, running the DeepPurpose models, implementing negative sample generation, and training VAENet.

R.W. contributed to writing the manuscript, generating the predictions for the network configuration model, designing and training VecNet and VAENet.

Z.S. contributed to training and testing of all the deep learning models, and designing the Siamese model.

D.G. contributed to the data curation and preparation, and performed the gene phylogeny study.

R.Y., T.E.R., and A.L.B. have provided guidance on designing the experiments and writing the manuscript.

G.M. conceived the project, developed the duplex configuration model, designed experiments to identify the emergence of topological shortcuts, contributed to data preparation, data analysis, and writing the manuscript.

Competing Interests

A.L.B. is the founder of Scipher Medicine and Foodome companies that explore the use of network-based tools in health, and Datapolis, that focuses on urban data.

Materials & Correspondence

Correspondence and requests for materials should be addressed to G.M.

Data and Code availability

The data and code that support the findings of this study are openly available at our GitHub page: <https://github.com/ChatterjeeAyan/AI-Bind>.

Top binding predictions from AI-Bind's VecNet on the COVID-19 related proteins, arranged in the descending order of predicted probabilities and validated by auto-docking: <https://github.com/ChatterjeeAyan/AI-Bind/blob/main/Validation/Predictions.csv>.

References

- [1] Hughes, J., Rees, S., Kalindjian, S. & Philpott, K. Principles of early drug discovery. *British Journal of Pharmacology* **162**, 1239–1249 (2011). URL <https://doi.org/10.1111/j.1476-5381.2010.01127.x>.
- [2] Thafar, M., Raies, A. B., Albaradei, S., Essack, M. & Bajic, V. B. Comparison study of computational prediction tools for drug-target binding affinities. *Frontiers in Chemistry* **7** (2019). URL <https://doi.org/10.3389/fchem.2019.00782>.
- [3] U.S. Food & Drug Administration. The Drug Development Process. URL <https://www.fda.gov/patients/learn-about-drug-and-device-approvals/drug-development-process>.
- [4] Hollingsworth, S. A. & Dror, R. O. Molecular dynamics simulation for all. *Neuron* **99**, 1129–1143 (2018). URL <https://doi.org/10.1016/j.neuron.2018.08.011>.
- [5] Vivo, M. D., Masetti, M., Bottegoni, G. & Cavalli, A. Role of Molecular Dynamics and Related Methods in Drug Discovery. *Journal of Medicinal Chemistry* **59**, 4035–4061 (2016). URL <https://pubs.acs.org/doi/full/10.1021/acs.jmedchem.5b01684>.
- [6] Chen, H., Engkvist, O., Wang, Y., Olivecrona, M. & Blaschke, T. The rise of deep learning in drug discovery. *Drug Discovery Today* **23**, 1241–1250 (2018). URL <https://doi.org/10.1016/j.drudis.2018.01.039>.
- [7] Jumper, J. *et al.* Highly accurate protein structure prediction with AlphaFold **596**, 583–589 (2021). URL <https://doi.org/10.1038/s41586-021-03819-2>.
- [8] Huang, K. *et al.* DeepPurpose: a deep learning library for drug–target interaction prediction. *Bioinformatics* (2020). URL <https://doi.org/10.1093/bioinformatics/btaa1005>.
- [9] Zhang, H. *et al.* DeepBindPoc: a deep learning method to rank ligand binding pockets using molecular vector representation. *PeerJ* **8**, e8864 (2020). URL <https://doi.org/10.7717/peerj.8864>.
- [10] Huang, G., Liu, Z., van der Maaten, L. & Weinberger, K. Q. Densely connected convolutional networks (2018). 1608.06993.
- [11] Verma, N. *et al.* SSnet: A deep learning approach for protein-ligand interaction prediction (2019). URL <https://doi.org/10.1101/2019.12.20.884841>.

- [12] Cui, Y., Dong, Q., Hong, D. & Wang, X. Predicting protein-ligand binding residues with deep convolutional neural networks. *BMC Bioinformatics* **20** (2019). URL <https://doi.org/10.1186/s12859-019-2672-1>.
- [13] Zhao, J., Cao, Y. & Zhang, L. Exploring the computational methods for protein-ligand binding site prediction. *Computational and Structural Biotechnology Journal* **18**, 417–426 (2020). URL <https://doi.org/10.1016/j.csbj.2020.02.008>.
- [14] Xia, C.-Q., Pan, X. & Shen, H.-B. Protein–ligand binding residue prediction enhancement through hybrid deep heterogeneous learning of sequence and structure data. *Bioinformatics* **36**, 3018–3027 (2020). URL <https://doi.org/10.1093/bioinformatics/btaa110>.
- [15] Wishart, D. S. *et al.* DrugBank: a knowledgebase for drugs, drug actions and drug targets. *Nucleic Acids Research* **36**, D901–D906 (2007). URL <https://doi.org/10.1093/nar/gkm958>. https://academic.oup.com/nar/article-pdf/36/suppl_1/D901/18782085/gkm958.pdf.
- [16] Gilson, M. K. *et al.* BindingDB in 2015: A public database for medicinal chemistry, computational chemistry and systems pharmacology. *Nucleic Acids Research* **44**, D1045–D1053 (2015). URL <https://doi.org/10.1093/nar/gkv1072>. <https://academic.oup.com/nar/article-pdf/44/D1/D1045/9482229/gkv1072.pdf>.
- [17] Richard, A. M. *et al.* The tox21 10k compound library: Collaborative chemistry advancing toxicology. *Chemical Research in Toxicology* **0**, null (0). URL <https://doi.org/10.1021/acs.chemrestox.0c00264>. PMID: 33140634, <https://doi.org/10.1021/acs.chemrestox.0c00264>.
- [18] Davies, M. *et al.* ChEMBL web services: streamlining access to drug discovery data and utilities. *Nucleic Acids Research* **43**, W612–W620 (2015). URL <https://doi.org/10.1093/nar/gkv352>.
- [19] Davis, M. I. *et al.* Comprehensive analysis of kinase inhibitor selectivity. *Nature Biotechnology* **29**, 1046–1051 (2011). URL <https://doi.org/10.1038/nbt.1990>.
- [20] Tang, J. *et al.* Drug target commons: A community effort to build a consensus knowledge base for drug-target interactions. *Cell Chemical Biology* **25**, 224–229.e2 (2018). URL <https://doi.org/10.1016/j.chembiol.2017.11.009>.
- [21] Barabási, A.-L. *Network Science* (Cambridge University Press, 2016).

- [22] Barabási, A.-L. & Albert, R. Emergence of scaling in random networks **286**, 509–512 (1999). URL <https://doi.org/10.1126/science.286.5439.509>.
- [23] Alstott, J., Bullmore, E. & Plenz, D. powerlaw: A python package for analysis of heavy-tailed distributions **9**, e85777 (2014). URL <https://doi.org/10.1371/journal.pone.0085777>.
- [24] Yang, J., Shen, C. & Huang, N. Predicting or pretending: Artificial intelligence for protein–ligand interactions lack of sufficiently large and unbiased datasets. *Frontiers in Pharmacology* **11** (2020). URL <https://doi.org/10.3389/fphar.2020.00069>.
- [25] Hu, F., Jiang, J., Wang, D., Zhu, M. & Yin, P. Multi-PLI: interpretable multi-task deep learning model for unifying protein–ligand interaction datasets. *Journal of Cheminformatics* **13** (2021). URL <https://doi.org/10.1186/s13321-021-00510-6>.
- [26] van Laarhoven, T., Nabuurs, S. B. & Marchiori, E. Gaussian interaction profile kernels for predicting drug–target interaction. *Bioinformatics* **27**, 3036–3043 (2011). URL <https://doi.org/10.1093/bioinformatics/btr500>.
- [27] Öztürk, H., Ozkirimli, E. & Özgür, A. A comparative study of SMILES-based compound similarity functions for drug-target interaction prediction. *BMC Bioinformatics* **17** (2016). URL <https://doi.org/10.1186/s12859-016-0977-x>.
- [28] Geirhos, R. *et al.* Shortcut learning in deep neural networks. *Nature Machine Intelligence* **2**, 665–673 (2020). URL <https://doi.org/10.1038/s42256-020-00257-z>.
- [29] Lee, A. A., Brenner, M. P. & Colwell, L. J. Predicting protein–ligand affinity with a random matrix framework. *Proceedings of the National Academy of Sciences* **113**, 13564–13569 (2016). URL <https://doi.org/10.1073/pnas.1611138113>.
- [30] Wang, Z., Liang, L., Yin, Z. & Lin, J. Improving chemical similarity ensemble approach in target prediction. *Journal of Cheminformatics* **8** (2016). URL <https://doi.org/10.1186/s13321-016-0130-x>.
- [31] Weininger, D. SMILES, a chemical language and information system. 1. introduction to methodology and encoding rules. *Journal of Chemical Information and Modeling* **28**, 31–36 (1988). URL <https://doi.org/10.1021/ci00057a005>.
- [32] Newman, M. *Networks: An Introduction* (OUP Oxford, 2010).

- [33] Menichetti, G., Remondini, D., Panzarasa, P., Mondragón, R. J. & Bianconi, G. Weighted multiplex networks. *PLoS ONE* **9**, e97857 (2014). URL <https://doi.org/10.1371/journal.pone.0097857>.
- [34] Menichetti, G. & Remondini, D. Entropy of a network ensemble: definitions and applications to genomic data. *Theor Biol Forum* **107**, 77–87 (2014).
- [35] Kim, S. *et al.* PubChem in 2021: new data content and improved web interfaces **49**, D1388–D1395 (2020). URL <https://doi.org/10.1093/nar/gkaa971>.
- [36] Pdb database. www.rcsb.org/.
- [37] and Alex Bateman *et al.* UniProt: the universal protein knowledgebase in 2021 **49**, D480–D489 (2020). URL <https://doi.org/10.1093/nar/gkaa1100>.
- [38] Stelzer, G. *et al.* The GeneCards suite: From gene data mining to disease genome sequence analyses **54** (2016). URL <https://doi.org/10.1002/cpbi.5>.
- [39] Jaeger, S., Fulle, S. & Turk, S. Mol2vec: Unsupervised machine learning approach with chemical intuition. *Journal of Chemical Information and Modeling* **58**, 27–35 (2018). URL <https://doi.org/10.1021/acs.jcim.7b00616>.
- [40] Asgari, E. & Mofrad, M. R. K. Continuous distributed representation of biological sequences for deep proteomics and genomics. *PLOS ONE* **10**, e0141287 (2015). URL <https://doi.org/10.1371/journal.pone.0141287>.
- [41] Haykin, S. *Neural networks: a comprehensive foundation* (Prentice Hall PTR, 1994).
- [42] Trott, O. & Olson, A. J. AutoDock vina: Improving the speed and accuracy of docking with a new scoring function, efficient optimization, and multithreading. *Journal of Computational Chemistry* NA–NA (2009). URL <https://doi.org/10.1002/jcc.21334>.
- [43] Gysi, D. M. *et al.* Network medicine framework for identifying drug-repurposing opportunities for COVID-19 **118**, e2025581118 (2021). URL <https://doi.org/10.1073/pnas.2025581118>.
- [44] Gordon, D. E. *et al.* A SARS-CoV-2 protein interaction map reveals targets for drug repurposing. *Nature* **583**, 459–468 (2020). URL <https://doi.org/10.1038/s41586-020-2286-9>.

- [45] Smith, R. D., Engdahl, A. L., Dunbar, J. B. & Carlson, H. A. Biophysical limits of protein–ligand binding. *Journal of Chemical Information and Modeling* **52**, 2098–2106 (2012). URL <https://doi.org/10.1021/ci200612f>.
- [46] Jeon, S. *et al.* Identification of antiviral drug candidates against SARS-CoV-2 from FDA-approved drugs. *Antimicrobial Agents and Chemotherapy* **64** (2020). URL <https://doi.org/10.1128/aac.00819-20>.
- [47] Dey, S. K. *et al.* Suramin, penciclovir, and anidulafungin exhibit potential in the treatment of COVID-19 via binding to nsp12 of SARS-CoV-2. *Journal of Biomolecular Structure and Dynamics* 1–17 (2021). URL <https://doi.org/10.1080/07391102.2021.2000498>.
- [48] Kondo, T., Watanabe, M. & Hatakeyama, S. TRIM59 interacts with ECSIT and negatively regulates NF- κ b and IRF-3/7-mediated signal pathways. *Biochemical and Biophysical Research Communications* **422**, 501–507 (2012). URL <https://doi.org/10.1016/j.bbrc.2012.05.028>.
- [49] Li, S., Wang, L., Berman, M., Kong, Y.-Y. & Dorf, M. E. Mapping a dynamic innate immunity protein interaction network regulating type i interferon production. *Immunity* **35**, 426–440 (2011). URL <https://doi.org/10.1016/j.immuni.2011.06.014>.
- [50] Dr. duke’s phytochemical and ethnobotanical databases, u.s. department of agriculture. <https://phytochem.nal.usda.gov/phytochem/search>.
- [51] Kotfis, K. *et al.* COVID-19—the potential beneficial therapeutic effects of spironolactone during SARS-CoV-2 infection. *Pharmaceuticals* **14**, 71 (2021). URL <https://doi.org/10.3390/ph14010071>.
- [52] Cadegiani, F. A., Goren, A., Wambier, C. G. & McCoy, J. Azithromycin with nitazoxanide, hydroxychloroquine or ivermectin, with or without dutasteride, for early stage covid-19: an open-label prospective observational study in males with mild-to-moderate covid-19 (the pre-androCoV male trial). (2020).
- [53] Pawelczyk, A. & Zaprutko, L. Anti-COVID drugs: repurposing existing drugs or search for new complex entities, strategies and perspectives. *Future Medicinal Chemistry* **12**, 1743–1757 (2020). URL <https://doi.org/10.4155/fmc-2020-0204>.
- [54] Carino, A. *et al.* Hijacking SARS-CoV-2/ACE2 receptor interaction by natural and semi-synthetic steroidal agents acting on functional pockets on the receptor binding domain. *Frontiers in Chemistry* **8** (2020). URL <https://doi.org/10.3389/fchem.2020.572885>.

- [55] Kumar, A. *et al.* Identification of phytochemical inhibitors against main protease of COVID-19 using molecular modeling approaches. *Journal of Biomolecular Structure and Dynamics* **39**, 3760–3770 (2020). URL <https://doi.org/10.1080/07391102.2020.1772112>.
- [56] Joh, E.-H., Gu, W. & Kim, D.-H. Echinocystic acid ameliorates lung inflammation in mice and alveolar macrophages by inhibiting the binding of LPS to TLR4 in NF- κ b and MAPK pathways. *Biochemical Pharmacology* **84**, 331–340 (2012). URL <https://doi.org/10.1016/j.bcp.2012.04.020>.
- [57] Joh, E.-H., Jeong, J.-J. & Kim, D.-H. Inhibitory effect of echinocystic acid on 12-o-tetradecanoylphorbol-13-acetate-induced dermatitis in mice. *Archives of Pharmacal Research* **37**, 225–231 (2013). URL <https://doi.org/10.1007/s12272-013-0092-8>.
- [58] Ryu, S. *et al.* Echinocystic acid isolated from eclipta prostrata suppresses lipopolysaccharide-induced iNOS, TNF- α , and IL-6 expressions via NF- κ b inactivation in RAW 264.7 macrophages. *Planta Medica* **79**, 1031–1037 (2013). URL <https://doi.org/10.1055/s-0032-1328767>.
- [59] Tong, X., Lin, S., Fujii, M. & Hou, D.-X. Echinocystic acid induces apoptosis in HL-60 cells through mitochondria-mediated death pathway. *Cancer Letters* **212**, 21–32 (2004). URL <https://doi.org/10.1016/j.canlet.2004.03.035>.
- [60] ting Deng, Y., bo Kang, W., ning Zhao, J., Liu, G. & gao Zhao, M. Osteoprotective effect of echinocystic acid, a triterpene component from eclipta prostrata, in ovariectomy-induced osteoporotic rats. *PLOS ONE* **10**, e0136572 (2015). URL <https://doi.org/10.1371/journal.pone.0136572>.
- [61] Heaven, W. D. The way we train ai is fundamentally flawed. *Technology Review* (2020). URL <https://www.technologyreview.com/2020/11/18/1012234/training-machine-learning-broken-real-world-heath-nlp-computer-vision/>.
- [62] Guney, E., Menche, J., Vidal, M. & Barábasi, A.-L. Network-based in silico drug efficacy screening. *Nature Communications* **7** (2016). URL <https://doi.org/10.1038/ncomms10331>.
- [63] do Valle, Í. F. *et al.* Network integration of multi-tumouromics data suggests novel targeting strategies. *Nature Communications* **9** (2018). URL <https://doi.org/10.1038/s41467-018-06992-7>.

- [64] Ferreira de Freitas, R. & Schapira, M. A systematic analysis of atomic protein-ligand interactions in the PDB. *Medchemcomm* **8**, 1970–1981 (2017).
- [65] Satorras, V. G., Hoogeboom, E., Fuchs, F. B., Posner, I. & Welling, M. E (n) equivariant normalizing flows for molecule generation in 3d. *arXiv preprint arXiv:2105.09016* (2021).
- [66] Fuchs, F. B., Worrall, D. E., Fischer, V. & Welling, M. Se (3)-transformers: 3d rotation equivariant attention networks. *arXiv preprint arXiv:2006.10503* (2020).
- [67] Jumper, J. *et al.* Highly accurate protein structure prediction with alphafold. *Nature* **596**, 583–589 (2021).
- [68] Finan, C. *et al.* The druggable genome and support for target identification and validation in drug development. *Science Translational Medicine* **9**, eaag1166 (2017). URL <https://doi.org/10.1126/scitranslmed.aag1166>.
- [69] Gorgulla, C. *et al.* An open-source drug discovery platform enables ultra-large virtual screens. *Nature* **580**, 663–668 (2020). URL <https://doi.org/10.1038/s41586-020-2117-z>.
- [70] Heller, S. R., McNaught, A., Pletnev, I., Stein, S. & Tchekhovskoi, D. InChI, the IUPAC international chemical identifier. *Journal of Cheminformatics* **7** (2015). URL <https://doi.org/10.1186/s13321-015-0068-4>.
- [71] Menichetti, G., Bianconi, G., Castellani, G., Giampieri, E. & Remondini, D. Multiscale characterization of ageing and cancer progression by a novel network entropy measure. *Mol. BioSyst.* **11**, 1824–1831 (2015). URL <http://dx.doi.org/10.1039/C5MB00143A>.
- [72] Mikolov, T., Sutskever, I., Chen, K., Corrado, G. S. & Dean, J. Distributed representations of words and phrases and their compositionality. In *Advances in neural information processing systems*, 3111–3119 (2013).
- [73] Rogers, D. & Hahn, M. Extended-connectivity fingerprints. *Journal of Chemical Information and Modeling* **50**, 742–754 (2010). URL <https://doi.org/10.1021/ci100050t>.
- [74] Doersch, C. Tutorial on variational autoencoders. *arXiv preprint arXiv:1606.05908* (2016). URL <https://arxiv.org/abs/1606.05908>.
- [75] Irwin, J. J., Sterling, T., Mysinger, M. M., Bolstad, E. S. & Coleman, R. G. ZINC: A free tool to discover chemistry for biology. *Journal of Chemical Information and Modeling* **52**, 1757–1768 (2012). URL <https://doi.org/10.1021/ci3001277>.

- [76] Koch, G., Zemel, R. & Salakhutdinov, R. Siamese neural networks for one-shot image recognition. In *ICML deep learning workshop*, vol. 2 (Lille, 2015).

Table 1: **BindingDB Training Data for DeepPurpose.** Most ligands and proteins in DeepPurpose training data have either binding or non-binding annotations, which creates imbalance in the degree ratio (see Eq. 1).

Node Type	Has Only Positive Annotations	Has Only Negative Annotations	Has both annotations	Total Node Count
Ligand	3,084	6,539	793	10,416
Protein	168	556	667	1,391

Table 2: **DeepPurpose and Duplex Configuration Model Performances on BindingDB dataset.** DeepPurpose and the duplex configuration model perform well in both transductive and inductive tests on the benchmark BindingDB data. Both models fail to achieve good performance in the inductive test, i.e., while predicting over both unseen proteins and ligands.

Model	Transductive		Semi-inductive		Inductive	
	AUROC	AUPRC	AUROC	AUPRC	AUROC	AUPRC
DeepPurpose	0.82 ± 0.003	0.48 ± 0.004	0.76 ± 0.036	0.69 ± 0.064	0.60 ± 0.066	0.42 ± 0.063
Config. Model	0.83 ± 0.009	0.5 ± 0.011	0.77 ± 0.048	0.71 ± 0.065	0.50 ± 0.00	0.30 ± 0.034

Table 3: **Assigning SMILES and Amino Acid Sequences Randomly.** A random reshuffle of SMILES and amino acid sequences does not affect the performance of DeepPurpose. This outcome suggests the limitation of DeepPurpose in learning chemical structures.

Version	AUROC	AUPRC
Original	0.85 ± 0.005	0.64 ± 0.008
Randomized	0.85 ± 0.005	0.63 ± 0.008

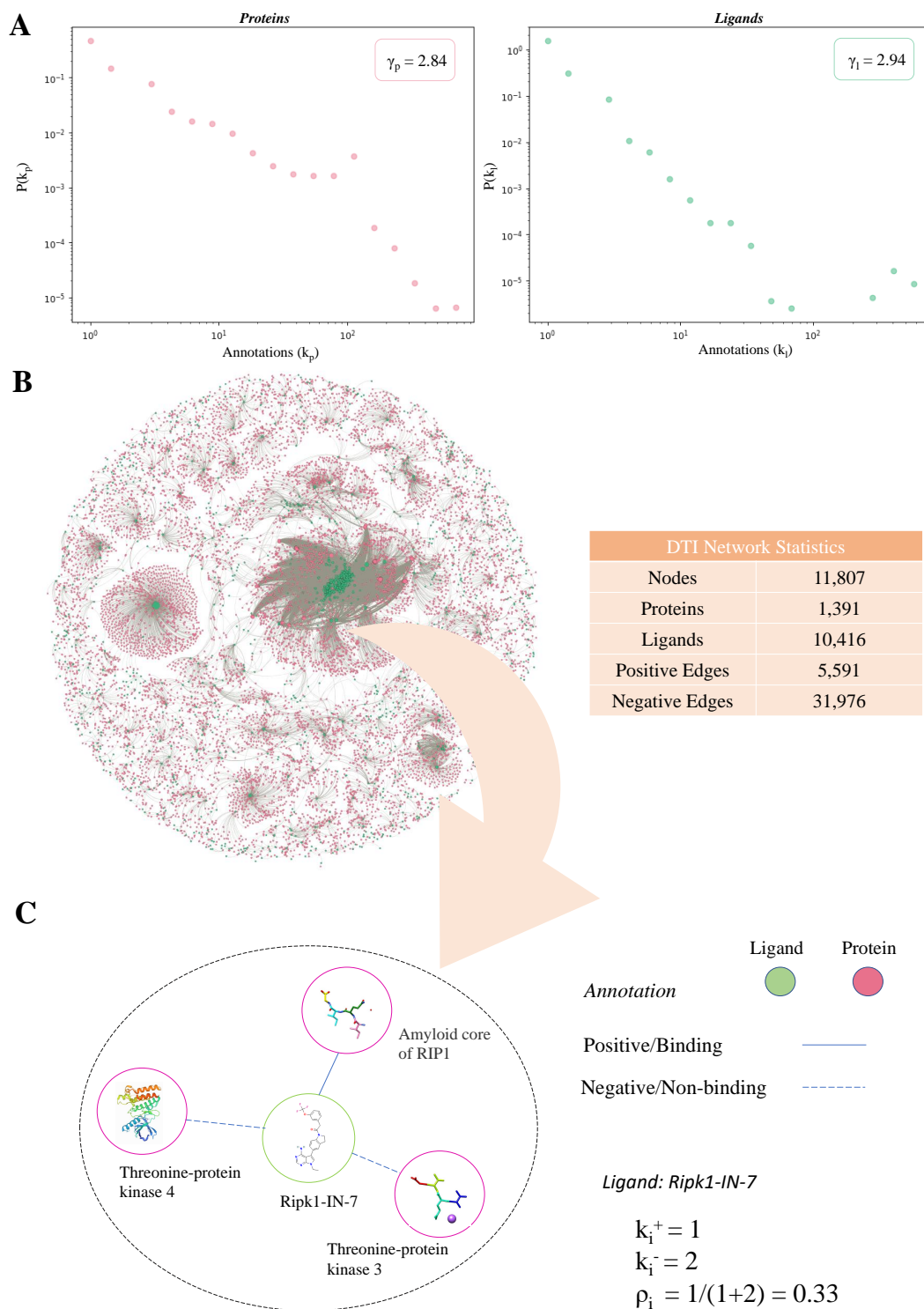


Figure 1: Drug-target Interaction Network. (A) Distributions of the number of annotations in the benchmark BindingDB data are shown in double logarithmic axes (log-log plot), indicate that $P(k_p)$ and $P(k_l)$ are well approximated by power law for both proteins and ligands, with approximate degree exponents $\gamma_p = 2.84$ and $\gamma_l = 2.94$, respectively. (B) The drug-target interaction network used to train the DeepPurpose models, consisting of 10,416 ligands and 1,391 protein targets. Ligands and proteins are represented by green and pink nodes, respectively. (C) Network neighborhood of the ligand Ripk1-IN-7. Solid links represent positive or binding annotations, while dashed links refer to negative or non-binding annotations. Ripk1-IN-7 has one positive and two negative annotations in the training data, implying a degree ratio ρ of 0.33.

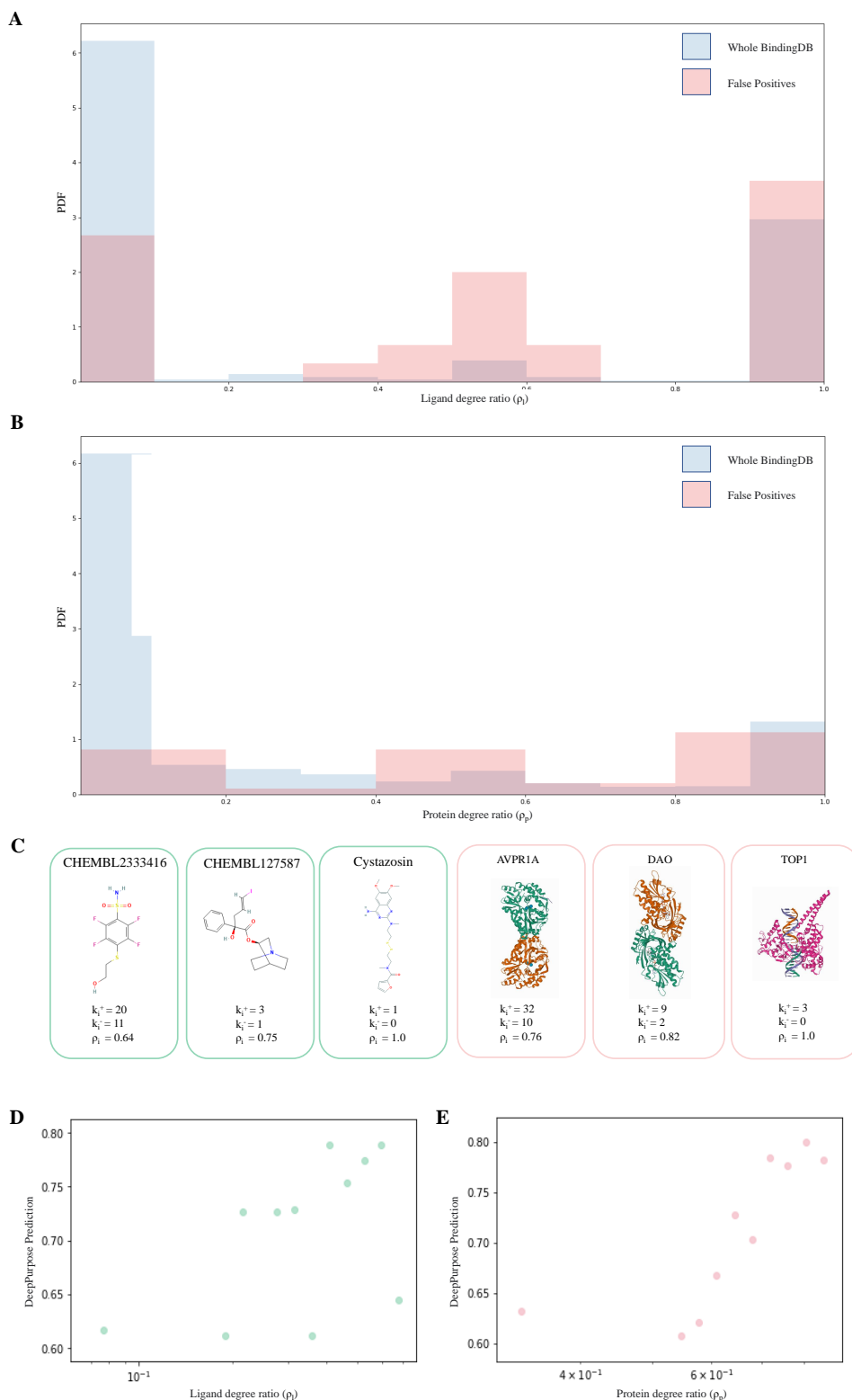


Figure 2: Annotation bias in DeepPurpose predictions. (A)-(B) The distributions of degree ratios for proteins and ligands in the original DeepPurpose training set (in a fold from the 5 fold cross-validation). Degree ratio defined in Eq. 1 refers to the ratio of positive annotations to the total annotations for a given node in the protein-ligand interaction network. Nodes contributing to the top 100 false positive predictions in the test set have higher degree ratios. (C) Examples of proteins and ligands with large degree ratios and contributing to false positive predictions. (D)-(E) Proteins and ligands with higher degree ratios tend to have higher binding predictions in DeepPurpose.

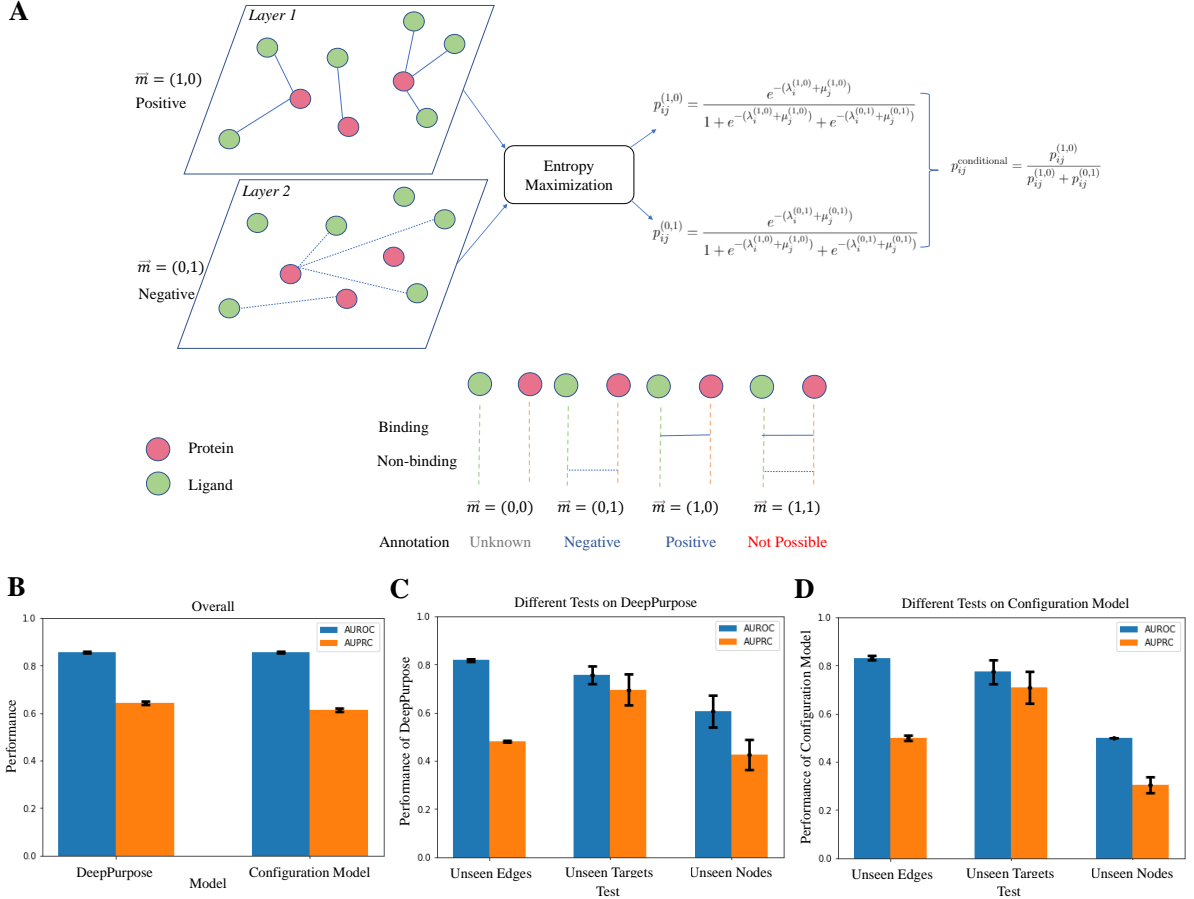


Figure 3: Comparing DeepPurpose and the Duplex Configuration Model. (A) The duplex configuration model includes two layers corresponding to binding and non-binding annotations. Positive and negative link probabilities are determined by entropy maximization (see Methods), and used to estimate the conditional probability in transductive (Eq. 7), semi-inductive (Eq. 8), and inductive (Eq. 9) scenario. (B)-(D) The configuration model achieves similar test performance as DeepPurpose on the the benchmark BindingDB data in a 5-fold cross-validation. Breakdown of performances shows good predictive performance on unseen edges and unseen targets. But the same models have poor predictive performance on unseen nodes.

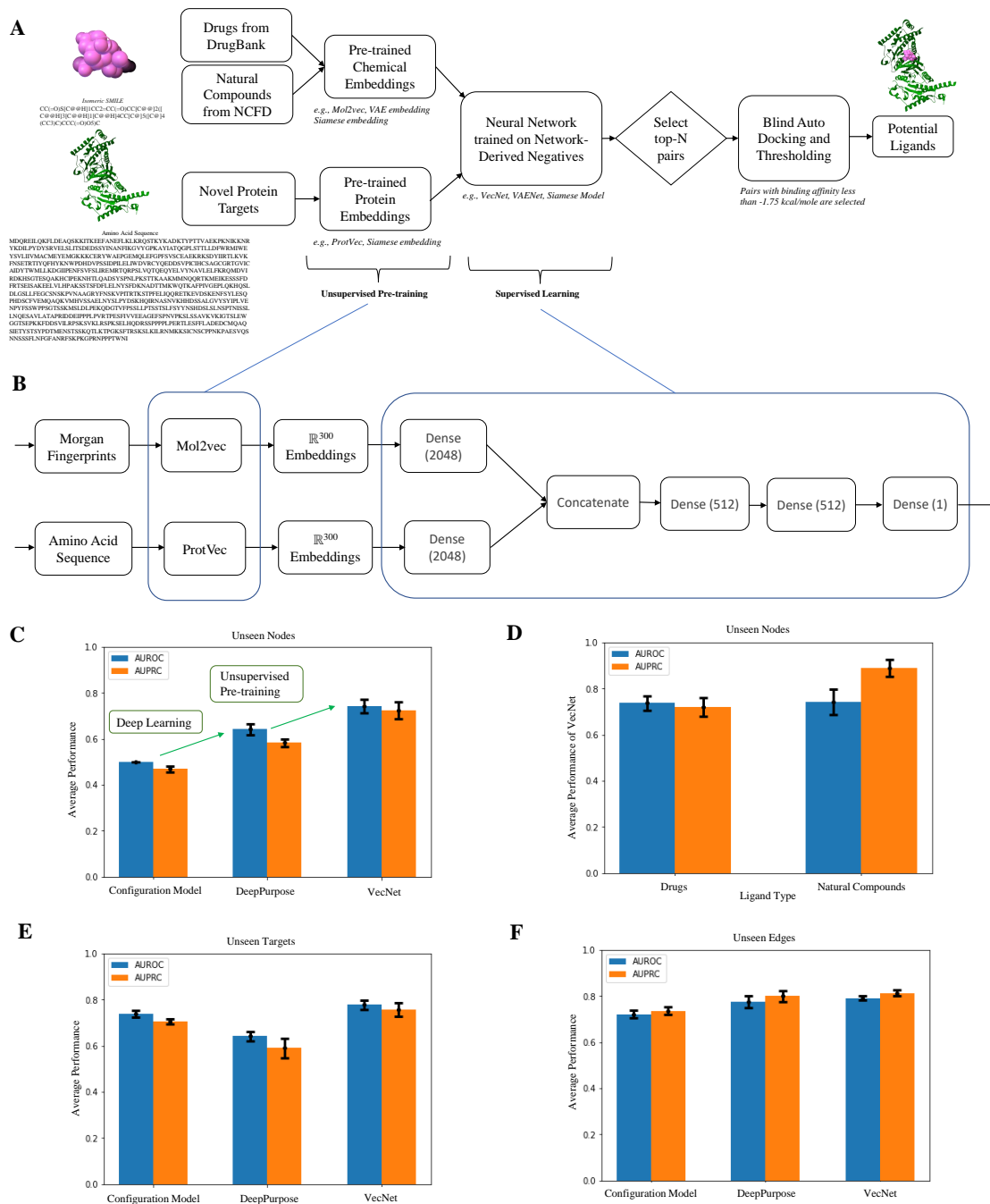


Figure 4: AI-Bind pipeline: VecNet Performance and Validation. (A) AI-Bind pipeline generates embeddings for ligands (drugs and natural compounds) and proteins using unsupervised pre-training. These embeddings are used to train the deep models. Top predictions are validated using auto-docking simulations and are used as potential binders to test experimentally. (B) AI-Bind’s VecNet architecture uses Mol2vec and ProtVec for generating the node embeddings. VecNet is trained in a 5-fold cross-validation set-up. Averaged prediction over the 5 folds is used as the final output of VecNet. (C)-(F) 5-fold cross-validation performance of VecNet, DeepPurpose, and Configuration Model. All the models perform similarly in case of predicting binding for unseen edges and unseen targets. The advantage of using deep learning and unsupervised pre-training is observed in the case of unseen nodes (inductive test). AI-Bind’s VecNet is the best performing model across all the scenarios. Additionally, we observe similar performance of VecNet for both drugs and natural compounds.

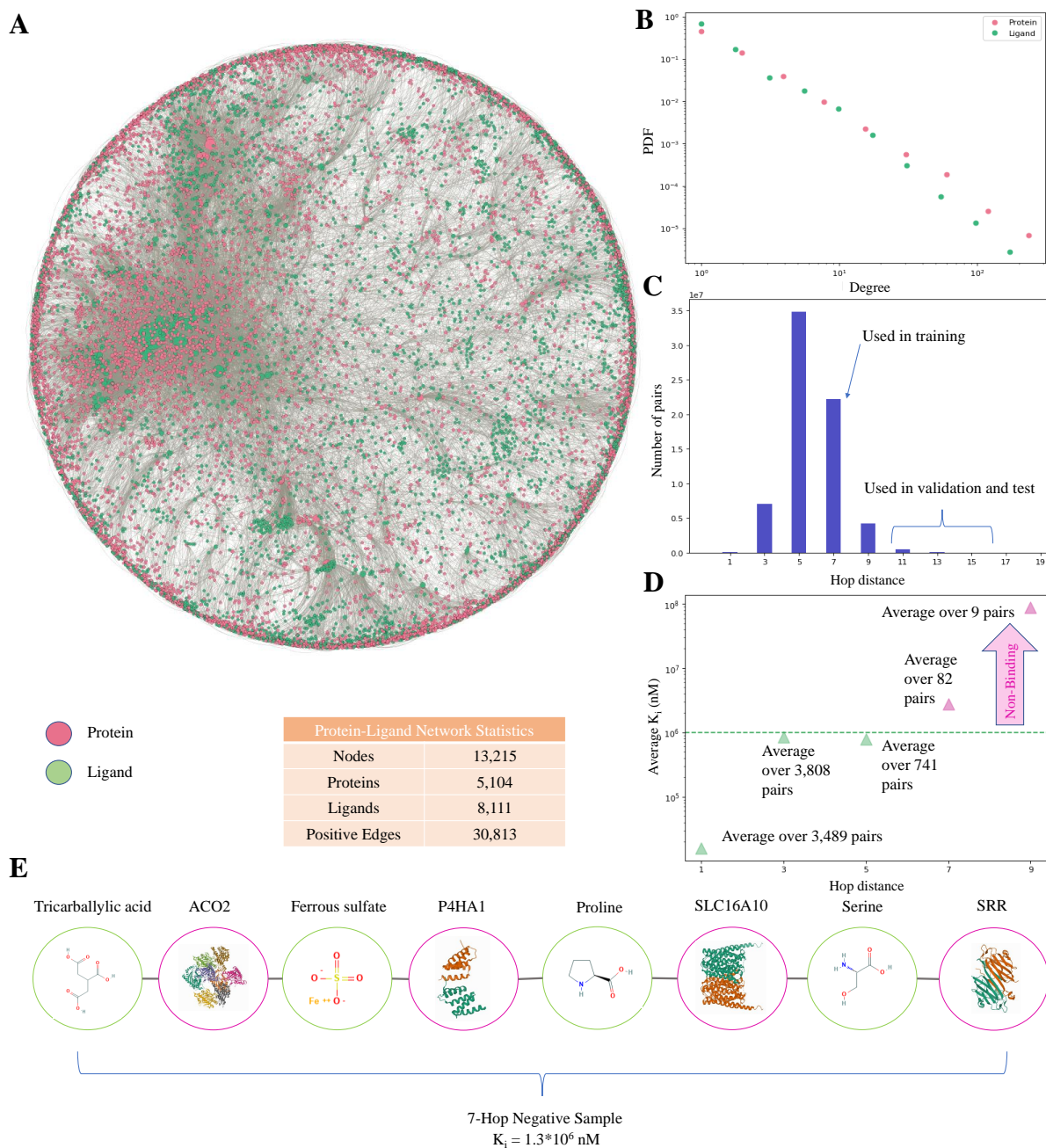
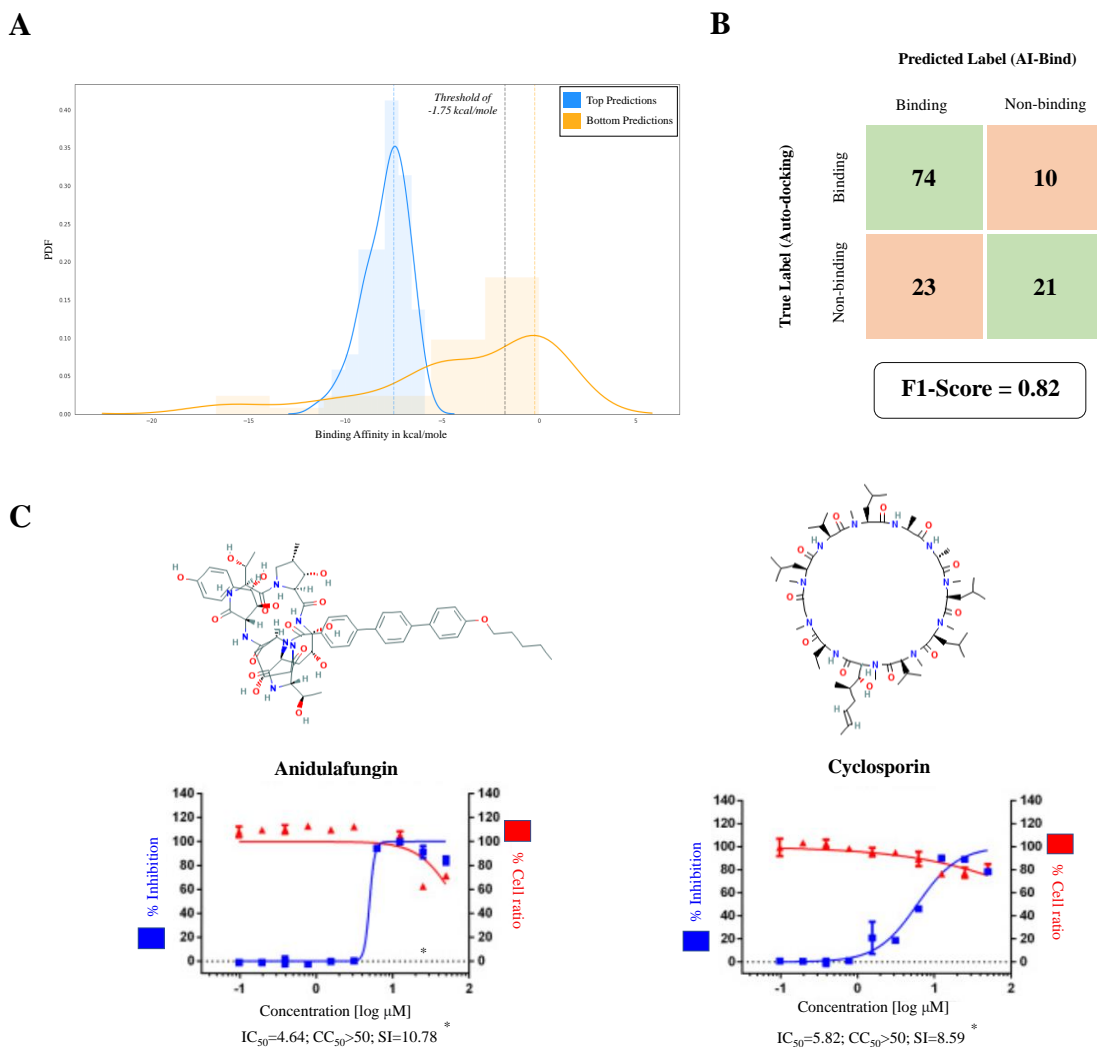


Figure 5: Network-Derived Negatives. (A) Protein-ligands bipartite network consisting of only binding (positive) annotations for drugs and natural compounds. (B) Degree distributions of ligands and proteins are fat-tailed in nature. (C) Shortest-path length distribution capturing all possible protein-ligand pairs. We use protein-ligand pairs with shortest path distance of 7 for training, while absolute negatives obtained from BindingDB and pairs with shortest path distances ≥ 11 are used for validation and test. (D) Average experimental kinetic constant as a function of the shortest path distance. Higher path distance corresponds to higher K_i in BindingDB. Beyond 7 hops, the expected constant exceeds the binding threshold of 10^6 nM. (E) An example of a protein-ligand pair which is 7 hops apart and is used as a negative sample in the AI-Bind training set.



*Adapted from Jeon, S. et al. Identification of antiviral drug candidates against SARS-CoV-2 from FDA-approved drugs. *Antimicrobial Agents and Chemotherapy* 64 (2020). URL <https://doi.org/10.1128/aac.00819-20>. Adapted with permission.

Figure 6: Validating AI-Bind predictions with AutoDocking. (A) Distribution of binding affinities for top and bottom 100 predictions made by AI-Bind's VecNet over viral and human proteins associated with COVID-19. We ran auto-docking on top 84 predictions and bottom 44 predictions. We observe that the top binding predictions of AI-Bind show lower binding energies (better binding) compared to the bottom predictions. Considering the binding threshold of -1.75 kcal/mole, 88% of the top predicted pairs by AI-Bind are inline with the auto-docking simulations. (B) We construct the confusion matrix for the top and bottom predictions from AI-Bind. We obtain the true labels using the threshold of -1.75 kcal/mole on the binding affinities from auto-docking. We observe that AI-Bind predictions produce excellent F1-Score, offering predictions significantly better than random selection. (C) Anidulafungin and Cyclosporin, two FDA approved anti-fungal agents predicted by AI-Bind, show potential antiviral activities against SARS-CoV-2, with IC_{50} values $4.64\mu M$ and $5.82\mu M$, respectively.

SUPPLEMENTARY INFORMATION

Table of Contents

S1	Emergence of topological shortcuts	32
S2	Naturally occurring ligands	35
S3	DeepPurpose false negative predictions due to annotation imbalance	36
S4	Databases	36
S4.1	DrugBank	36
S4.2	Drug Target Commons	36
S4.3	BindingDB	36
S4.4	Natural Compounds in Food Database	37
S5	7-hop threshold for network-derived negatives	37
S6	Novel deep learning models	38
S6.1	VecNet	39
S6.2	Siamese model	40
S6.3	VAENet	40
S7	Additional deep learning model results	41
S8	Validation using gene phylogeny and bias in false predictions	42
S9	Optimal representation of protein and ligand molecules	42
	Supplementary References	44

S1 Emergence of topological shortcuts

Decision rules learned by many machine learning (ML) models tend to perform well on benchmark datasets, but fail to generalize well when given never-before-seen data. Instead of learning generalizable patterns from features observed during training, these models leverage shortcuts in the data to maximize transductive performance, i.e., the performance on seen data [28]. In this section, we investigate how the properties of the network data used in training can drive ML models to learn topological shortcuts, rather than taking into account node features that would allow better generalizability to unseen data.

BindingDB data observations

First, we investigated the statistical properties of the training database used by DeepPurpose [8], a modeling pipeline offering state-of-the-art neural architectures to predict protein-ligand binding. The training data is based on all the records in BindingDB [79] characterized by a kinetic disassociation constant K_d . The distribution of the number of annotations per protein $P(k_p)$ is well fitted by a power law distribution using [23]

$$P(k_p) \sim k^{-\gamma_p}, \quad (10)$$

with $\gamma_p = 2.84$, $k_p^{min} = 1$, and $k_p^{max} = 1,426$ (Figure 1A in the main text). We observe similar results for the ligands, with $\gamma_l = 2.94$, $k_l^{min} = 1$, and $k_l^{max} = 1,161$.

A binary classification dataset from BindingDB using a threshold for K_d , with default threshold $30nM$. Protein-ligand pairs with $K_d < 30nM$ are binding or positive pairs, and everything else is labeled non-binding or negative. Overall, we observe that 16% of the records are labeled as positive, a characteristic of the database that we summarize as $p_{bind} = 0.16$, the probability to observe a binding annotation independently from the identity of the protein and the ligand.

Additionally, we observe that the number of annotations k per node and the average disassociation constant $\langle K_d \rangle$ across the related annotations are not independent but have weak negative rank correlations. In particular, for proteins we find $r_{Spearman}(k_p, \langle K_d \rangle) = -0.47$, and for ligands $r_{Spearman}(k_l, \langle K_d \rangle) = -0.29$ (Figure S1C, D).

Toy-model set-up

In order to test our hypotheses regarding the creation of topological shortcuts, we simulate synthetic network data we call the *toy model* (Figure S2). We create a duplex of unipartite networks with features inspired by the protein sample captured in BindingDB, as similar con-

siderations extend to bipartite networks. Specifically, we vary the degree distribution $P(k)$ and $r_{Spearman}(k, \langle K_d \rangle)$ to explore when the output of the duplex configuration model (Figure 3A, Methods in the main text) $\{p_{ij}^{conditional}\}$ from Eq. 7 in the main text becomes highly variable and thus informative, creating the potential for topological shortcuts. Simply, the closer $\{p_{ij}^{conditional}\}$ gets to a Naive Bayes classifier, the less attractive it will be for machine learning models learning a classification task as the predictions would provide similar information as random selection.

We generate random duplexes of unipartite networks with Poisson or power law degree distributions and different rank correlations $r_{Spearman}(k, \langle K_d \rangle)$ according to four different specifications:

- Poisson degree distribution with average degree $\langle k \rangle = 47$, and $r_{Spearman}(k, \langle K_d \rangle) \approx 0$;
- Poisson degree distribution with average degree $\langle k \rangle = 47$, and $r_{Spearman}(k, \langle K_d \rangle) \approx -0.47$;
- Power law degree distribution $P(k) \sim k^{-2.84}$, and $r_{Spearman}(k, \langle K_d \rangle) \approx 0$;
- Power law degree distribution $P(k) \sim k^{-2.84}$, and $r_{Spearman}(k, \langle K_d \rangle) \approx -0.47$.

We simulate samples of degree k and $\langle K_d \rangle$ with different correlations by leveraging the formalism of Gaussian copulas [81]. First, we generate two jointly distributed standard normal random variables x_1 and x_2 with the desired correlation. We then use their marginal CDFs U_1 and U_2 , respectively, to sample back k and $\langle K_d \rangle$ according to the distribution of choice. In particular, for the kinetic constants we constrain the overall mean $\langle \log(K_d) \rangle$ and standard deviation $\sigma(\log(K_d))$ observed in the original database, effectively making the simulated distribution log-normal. The sampled $\langle \log(K_d) \rangle^i$ represent the average binding strength for a given node i with degree k_i . For the selected node, we further sample k_i kinetic constants from a log-normal distribution with mean value for the logarithmic parameters $\log(\langle K_d \rangle^i)$ and standard deviation $\sigma_{\log(K_d)}^{k_i}$, i.e the expected standard deviation of the kinetic constants across the links for all nodes with degree equal to k_i in the original data. Then $K_d^{(i,j)}$ assigned to edge (i, j) is the geometric mean of the contribution K_d^i from node i and the contribution K_d^j from node j , i.e.,

$$K_d^{(i,j)} = \sqrt{K_d^i K_d^j}. \quad (11)$$

We select as threshold for $K_d^{(i,j)}$ the value for which 16% of the annotations become positive (binding), enforcing the constraint on the observed p_{bind} . Based on this threshold, we generate the duplex layers with positive and negative edges and calculate the multilink degree sequences, input to the configuration model (see Methods in the main text).

Mathematical formalism for the uncorrelated scenario

When $\langle K_d \rangle$ and k are independent, we can analytically derive the statistical behavior of positive degree k^+ , negative degree k^- , and degree ratio ρ (Eq. 1 in the main text). For each node, the probability of observing k^+ positive annotations out of k links is binomial

$$P(k^+|k) = \binom{k}{k^+} p_{bind}^{k^+} (1 - p_{bind})^{(k-k^+)}, \quad (12)$$

where p_{bind} encodes the percentage of positive records observed in the database.

The distribution of positive annotations k^+ for the whole database is then a compound distribution

$$P(k^+) = \int P(k) P(k^+|k) dk, \quad (13)$$

where $P(k)$ is the candidate probability distribution for the number of annotations k .

From the laws of total expectation and total variance we derive

$$\langle k^+ \rangle = p_{bind} \langle k \rangle, \quad (14)$$

$$\sigma^2(k^+) = p_{bind}(1 - p_{bind}) \langle k \rangle + p_{bind}^2 (\langle k^2 \rangle - \langle k \rangle^2), \quad (15)$$

where similar equations hold for k^- , with $(1 - p_{bind})$ replacing p_{bind} . When $P(k)$ is fat-tailed, $(\langle k^2 \rangle - \langle k \rangle^2)$ becomes dominant, and the random variable $k^+ \approx p_{bind} \langle k \rangle$. This formulation suggests that, even in the presence of fat-tailed $P(k)$, the lack of correlations between $\langle K_d \rangle$ and k would determine a distribution of degree ratio ρ well represented by the average

$$\langle \rho \rangle \approx \frac{\langle k^+ \rangle}{\langle k \rangle} = p_{bind}, \quad (16)$$

with noise determined by p_{bind} and $P(k)$. As the duplex configuration model constrains the degree ratio sequence $\{\rho_i\}$, the variability of $\{p_{ij}^{conditional}\}$ drops significantly in absence of correlation between $\langle K_d \rangle$ and k , bringing the model closer to a Naive Bayes classifier (Figure S3).

We can clearly derive the behavior of $p_{ij}^{conditional}$ in the case of *uncorrelated networks*, i.e., networks with no degree correlation and an upper bound for the maximum degree equal to $\sqrt{\langle k \rangle N}$, where N is the size of the unipartite network (Advanced Topics 7.B in [21]). In this

scenario the Lagrangian multipliers satisfy:

$$e^{-\lambda_i^{(1,0)}} = \frac{k_i^+}{\sqrt{\langle k^+ \rangle N}} \approx \frac{p_{bind} k_i}{\sqrt{p_{bind} \langle k \rangle N}}, \quad (17)$$

$$e^{-\lambda_i^{(0,1)}} = \frac{k_i^-}{\sqrt{\langle k^- \rangle N}} \approx \frac{(1 - p_{bind}) k_i}{\sqrt{(1 - p_{bind}) \langle k \rangle N}}, \quad (18)$$

$$p_{ij}^{(1,0)} = e^{-(\lambda_i^{(1,0)} + \lambda_j^{(1,0)})}, \quad (19)$$

$$p_{ij}^{(0,1)} = e^{-(\lambda_i^{(0,1)} + \lambda_j^{(0,1)})}. \quad (20)$$

It follows that Eq. 7 in the main text for $p_{ij}^{conditional}$ in the transductive test becomes independent from the identity of node i and j , as the product $k_i k_j$ simplifies, leading to $p_{ij}^{conditional} = p_{bind}$.

Observations

The duplex configuration model achieves the best performance when $P(k)$ follows a power-law, and k and $\langle K_d \rangle$ are negatively correlated. In absence of negative correlation, the performance drops, as $\{p_{ij}^{conditional}\}$ becomes more mean-centered. We observe low performances when $P(k)$ is Poisson, even in the presence of negative correlation, as the annotation distribution makes all nodes roughly equivalent. The worst performance is observed in case of a Poisson annotation distribution and no correlation, as the model is by definition the closest to a Naive Bayes classifier (for a summary of the performances see Table S1). According to these observations, annotation imbalance emerges as the combined effect of degree distribution and negative correlation between kinetic constants and degree, leading to potential topological shortcuts (Figure S3).

S2 Naturally occurring ligands

We extend the drug repurposing task to additional ligands which are not necessarily considered drugs but may nonetheless bind to protein targets. Specifically, we look into the *Natural Compounds in Food Database (NCFD)* (see Section S4.4), which contains food-borne natural compounds, some of which are potential protein binders. Although these ligands have known chemical structures, they lack adequate binding annotations for training ML models. Binding predictions for these ligands largely depend on comparing their chemical features to other ligands, for which more binding data is available. Figure S4 shows that the naturally occurring compounds in NCFD are larger in size and are more diverse in terms of atomic constituents compared to the drug molecules in DrugBank. This suggests that the binding prediction task on these natural compounds is challenging, which we tackle by maximizing the amount of training

data for these natural compounds, and pre-training the chemical embeddings on large chemical libraries.

S3 DeepPurpose false negative predictions due to annotation imbalance

A false negative prediction corresponds to a low binding probability output by the ML model for a protein-ligand pair which does, in fact, bind. In Figures S5A and S5B, we observe that DeepPurpose produces false negative predictions more often for ligands and proteins with low degree ratios. We notice the opposite for the false positives; nodes with high degree ratios contribute more to the false positive predictions in DeepPurpose predictions (see Figure 2 in the main text).

S4 Databases

AI-Bind combines data from four databases: DrugBank, Drug Target Commons (DTC), BindingDB, and Natural Compounds in Food Database (NCFD).

S4.1 DrugBank

DrugBank [15] consists of 7,307 drugs and 4,762 protein targets, which form 25,373 drug-target binding pairs. 167 of these drugs are found in NCFD, and we classify them as naturally occurring and food-borne. We consider all reported protein-ligand pairs from DrugBank as positive samples in our dataset, except 53 pairs which have kinetic constants $\geq 10^6 nM$ in BindingDB. The protein sequences included in DrugBank are derived from a wide variety of organisms, including human and different viruses.

S4.2 Drug Target Commons

We use Drug Target Commons (DTC) [20] for obtaining binding information related to the natural compounds in NCFD. The intersection of NCFD and DTC contains 1,820 natural ligands and 466 associated proteins.

S4.3 BindingDB

BindingDB [79] consists of protein-ligand pairs along with associated kinetic constants and physical conditions related to the reactions such as pH and temperature. We use BindingDB to extend the number of binding pairs in our training data, filter out the non-binding ones from DrugBank, and obtain absolute negative samples.

S4.4 Natural Compounds in Food Database

Multiple existing databases contain information about the compounds present in different food items. As a part of the Foodome project at Center for Complex Network Research (CCNR), we curated external databases like FooDB [85], Dictionary of Food Compounds (DFC) [86], and KNApSAcK [87] to gather information about the compounds in food. Metabolomic experiments were performed to further enrich the database. NCFD contains 20,700 compounds found in different food items, among which $\approx 19,000$ contain isomeric SMILES [31], a plain-text encoding of the chemical structures of each molecule¹. AI-Bind uses SMILES as input to its ML models for learning useful chemical embeddings.

Figure S6 shows the detailed breakdown of the protein-ligand binding pairs obtained from different databases.

S5 7-hop threshold for network-derived negatives

We use shortest path distances to generate negative samples. We consider the node pairs which have shortest path distance ≥ 7 in the network as non-binding. We derive this 7-hop threshold based on two observations. First, 7 hops is the minimum shortest path distance at which the average kinetic constant value is above the non-binding threshold of $10^6 nM$ (See Figure 5D in the main text). Second, 7 hops is small enough that the negative samples for a given node are not easily distinguishable from positive samples, making the learning task more complex, which helps to defeat shortcut learning in ML models. The latter observation is based on EigenSpokes [89] analysis, a network-based dimensionality reduction procedure inspired by Principal Component Analysis (PCA). Let A be the square adjacency matrix of the protein-ligand network. Since A is real symmetric, it is orthogonally diagonalizable. Let e_1, \dots, e_n be the eigenvectors of A sorted by eigenvalue magnitude $|\lambda_1| \geq |\lambda_2| \geq \dots \geq |\lambda_n|$. Given a node i , we write the row a_i of A in terms of the eigenbasis $a_i = u_{i1}e_1 + \dots + u_{in}e_n$. Truncating after the first 5 eigenvectors (with highest eigenvalue magnitudes) gives a low-dimensional embedding $\bar{u}_i = (u_{i1}, u_{i2}, u_{i3}, u_{i4}, u_{i5})$ of each node. The choice of 5 dimensions gives a useful low-dimensional embedding, while still capturing the most significant degrees of variation.

Now, consider a fixed protein i . Then ligands $\{j_1, j_2, \dots\}$ which bind to i (1-hop) have high magnitude and variance in this 5-dimensional space. On the other hand, ligands $\{k_1, k_2, \dots\}$

¹NCFD data was accessed on 7.14.2021. As this database undergoes constant change, we have included a description of the dataset at the time of download in the SI.

that are at a distance of 13 hops from i have \bar{u}_k very close to the origin (Table S2). When 13 hops is chosen as the threshold for negative samples, it would thus be trivial for ML models to distinguish nodes $\{j_1, j_2, \dots\}$ 1 hop away apart from nodes $\{k_1, k_2, \dots\}$ 13 hops away, resulting in shortcut learning. Indeed, the same low-degree ligands on the periphery of the network would become negative samples for all the proteins.

We observe a similar behavior for 11-hop and 9-hop thresholds. However, at 7 hops, we see significantly higher magnitude and variance in \bar{u}_k , indicating more diverse negative samples for each protein. In Figure S7A, we visualize (u_3, u_4) for ligands, colored based on the hop-distances from the example protein BPT4. We see that at shortest path distances ≥ 7 , most nodes are very close to the origin. In Figure S7B, we show the mean of all $\|\bar{u}_j\|$ values averaged over all pairs (i, j) of a given path length. Similarly to what we observed for BPT4, we observe a significant fall-off in magnitude as the shortest path length increases.

S6 Novel deep learning models

We observe that neural networks exploit the topology of the protein-ligand bipartite network used in training to achieve good performance, and lack node-level generalizability when trained in an end-to-end fashion. AI-Bind circumvents these issues by training its ML models in two phases. First, AI-Bind learns the node features using unsupervised pre-training, and then it separately trains its classifiers in a supervised manner to predict binding. To show that AI-Bind is not specific to a certain neural network architecture, we experiment with 3 two-phase networks: VecNet, Siamese model, and VAENet. AI-Bind first trains a neural network in an unsupervised manner to embed the nodes into a low-dimensional latent space, learning generalizable node representations based on the node features alone (chemical structures of ligands and amino acid sequences of proteins). For example, one of the AI-Bind architectures, VecNet, uses unsupervised node representations from Mol2vec [90] and ProtVec [40], which are trained separately from each other and from the protein-ligand bipartite network used in training. Mol2vec and ProtVec are both based on Word2Vec [92], and are designed to create low-dimensional vector representations which retain contextual information for “words” in “sentences”, where the “sentences” are formed by molecular sequence descriptions such as Morgan fingerprints [93] or protein sequences. In the second phase, these node representations are passed as input to a binding prediction network, which is trained in a supervised manner. In AI-Bind’s VecNet, the binding prediction network uses fully-connected layers and ReLU non-linearities.

The Siamese model uses triplet similarity to find a representation for the node (protein and

ligand) features based on their common bindings. The embeddings are then used as inputs to a multilayer perceptron, which learns bindings in a separate supervised training. The last of AI-Bind’s three models, VAENet, uses a Variational Auto-Encoder [94] in order to learn unsupervised ligand representations.

S6.1 VecNet

We use the pre-trained Mol2vec [39] and ProtVec [40] models for node representations. The pre-trained Mol2vec and ProtVec models create 300 and 100 dimensional embeddings for ligands and proteins, respectively. They are based on Word2Vec [72], and treat the Morgan fingerprints [73] and amino acid sequences as sentences in which substructure fingerprints (fragments) and trigrams are the words, respectively. They are trained in an unsupervised manner to create the representations independent of the binding information. Namely, they are trained to predict which words appear near each other in sentences.

Given a fingerprint x^0 and an amino acid sequence x^1 , we encode them using Mol2vec and ProtVec, and then pass them through a simple decoder. We experimented with different neural network architectures with differing number of layers (up to 6 dense layers) and number of neurons per layer (selected from powers of 2 starting at 128 to 2048) and picked one that performed best in inductive tests. This architecture is shown in Figure S8A.

More formally, VecNet computes :

$$\begin{aligned}\bar{x}^0 &= \text{mol2vec}(x^0) \in \mathbb{R}^{300}, & \bar{x}^1 &= \text{protvec}(x^1) \in \mathbb{R}^{100} \\ \tilde{x}^0 &= \text{ReLU}(W^0 \bar{x}^0) \in \mathbb{R}^{2048}, & \tilde{x}^1 &= \text{ReLU}(W^1 \bar{x}^1) \in \mathbb{R}^{2048}\end{aligned}$$

$$h^0 = \text{Concatenate}(\tilde{x}^0, \tilde{x}^1) \in \mathbb{R}^{4096}$$

$$h^1 = \text{ReLU}(W^2 h^0) \in \mathbb{R}^{512}$$

$$h^2 = \text{ReLU}(W^3 h^1) \in \mathbb{R}^{512}$$

$$\hat{y} = \sigma(W^4 h^2) \in [0, 1]$$

where σ is the sigmoid function and $\sigma(x) = \frac{1}{1+e^{-x}}$.

Prior use of Mol2Vec and ProtVec in binding prediction. Mol2Vec has previously been used for binding prediction, but only for pre-specified proteins [90], where the ML model is trained on one protein at a time. No information is encoded regarding the protein except for its binding scores with other chemicals in the training data. In contrast, AI-Bind’s VecNet attempts

to generalize for different proteins, which we encode using ProtVec. Jaeger et al. [90] also propose PCM2vec, in which they predict properties of proteins by concatenating Mol2Vec and ProtVec vectors for the same protein read in as a molecule and amino acid sequence, respectively. However, they do not attempt to combine these vectors for different inputs corresponding to a protein-ligand pair.

S6.2 Siamese model

The Siamese model uses one-shot learning to embed proteins and ligands into the same latent space [76]. For a given node, the Siamese model minimizes the Euclidean distances of that node from the nodes which bind to it, while maximizing the distances to the nodes which do not. This process is executed in triplets of the forms $\langle \text{protein, non-binding ligand, binding ligand} \rangle$. For the first kind, AI-Bind trains the network to maximize the Euclidean distance between the protein target and the non-binding ligand, while minimizing the distance of the target from the binding ligand (Figure S9A). AI-Bind uses these embeddings, generated by the Siamese architecture, to train a separate model for the downstream classification task of predicting binding. We studied the inductive test performance by changing the number of convolutional layers and the number of embedding dimensions. The final Siamese model consists of 4 convolutional layers and creates 128-dimensional output vectors. The classification network concatenates the embeddings for a protein and a ligand, and then passes it through two fully connected layers, similar to VecNet, to predict the binding probabilities (Figure S8C).

S6.3 VAENet

VAENet uses a Variational Auto-Encoder [74], an unsupervised learning technique, to embed ligands onto a latent space. Morgan fingerprints are directly fed into a convolutional neural network. The auto-encoder minimizes the loss of structural information while reconstructing the molecule back from the latent representation (Figure S9B). We generate 300-dimensional ligand embeddings using the auto-encoder, which is consistent with the dimensionality of the Mol2vec embeddings used in VecNet. The variational nature of this 300-dimensional space allows it to be continuous, allowing for better generalizability. We achieve this generalizability by using the re-parameterization trick from [100] to sample from the latent space, instead of directly connecting the latent space to the decoder. Having a generalizable continuous space allows us to map novel ligands into the latent space.

The downstream classification task is achieved by training a fully connected neural network on the concatenated embeddings generated from the Variational Auto-Encoder and ProtVec.

The non-end-to-end nature of this architecture ensures that the learned molecular features are independent from the classification task, which has a tendency to exploit shortcuts related to the topology of the protein-ligand interaction network.

S7 Additional deep learning model results

Table S3 contains the performances of AI-Bind’s novel deep learning architectures, a DeepPurpose baseline (Transformer-CNN), and the duplex network configuration model on the network-derived dataset. We also report the performances for models trained with randomized node features. This removes structural information about the proteins and ligands, helping us understand whether the deep learning models leverage structure to learn binding or take topological shortcuts. We observe that DeepPurpose’s performance does not change if the inputs are randomly shuffled, which suggests that DeepPurpose learns the topology of the protein-ligand interaction network instead of the node features.

In AI-Bind, network-derived negatives and unsupervised pre-training allow the deep learning models to learn binding patterns using the chemical structures instead of the topology of the protein-ligand interaction network. Thus, we observe diminished performance while using random features to make predictions for unseen nodes (inductive test). In this case network-derived negatives remove the annotation imbalance from the training data and prohibit the ML models from taking topological shortcuts.

Figure S10 shows the training curves averaged over 5 data splits (85 : 15 split to create train and validation-test datasets) for AI-Bind’s three novel models. We set the stopping criterion for training to maximize the inductive test performance (AUPRC) on the validation set. Figure S11 shows the F1-scores for the trained models relative to the classification threshold. We obtain the optimal threshold from this curve, which corresponds to the highest F1-score. This optimal threshold is used to obtain the binary labels from the predicted continuous outputs of the AI-Bind architectures. For AI-Bind’s VecNet, we obtain an optimal threshold of 0.09 (\pm 0.015) in the inductive test scenario. We observe a low optimal threshold as AI-Bind’s VecNet predicts high binding probability (p_{ij}^{VecNet}) for a few protein-ligand pairs, but we have roughly the same number of positive and negative samples in the test data. We recommend to use p_{ij}^{VecNet} values to select the top-N predictions, rather than using this optimal threshold to derive the binary labels for novel protein-ligand pairs absent in AI-Bind test data.

S8 Validation using gene phylogeny and bias in false predictions

As additional validation, we investigate if AI-Bind’s VecNet predictions are biased towards certain protein structures. The inductive test sets contain a total of 4,583 proteins which are unseen during training in different splits of the 5-fold cross-validation set-up. On 3,162 of these proteins, AI-Bind’s VecNet makes at least one false prediction, meaning that our model incorrectly labels at least one ligand as a binder which is not (false positive), or labels a ligand as non-binder which does, in fact, bind (false negative). Among these targets, we find that only 228 (5% of all the proteins) are indeed over-represented (proportions test [101]; p_{BH-fdr} -value ≤ 0.05), meaning that over half the predictions involving these proteins are false. To assess the nature of these false predictions, we test their bias for false positives or false negatives. We find that 168 proteins are biased towards false positive predictions, whereas 68 are biased towards false negatives (proportions test; p_{BH-fdr} -value ≤ 0.05).

To understand whether these biases are intrinsic to the evolutionary origins of certain proteins and if AI-Bind’s biases are associated with certain protein domains, we perform a phylogenetic analysis. We use MUSCLE [102], a tool for multiple protein sequence alignment, to understand the similarity between these 228 over-represented protein sequences. We observe only weak similarities between these over-represented proteins. We also reconstruct their phylogenetic tree using the neighbor joining tree method [103] on their amino acid sequences and visualize the results using `treeio` and `ggtree` R packages [104, 105]. The results suggest that the false predictions for AI-Bind’s VecNet have no bias towards any particular protein structure (Figure S12).

S9 Optimal representation of protein and ligand molecules

AI-Bind’s VecNet achieves the highest inductive performance, i.e., the performance on never-before-seen proteins and ligands. VecNet uses pre-trained Mol2vec (300-dimensional) and ProtVec (100-dimensional) embeddings. These embeddings encode the structural information from the whole protein and ligand molecules [90, 106]. However, protein-ligand binding is influenced by specific molecular properties, hence we focused on the structural features that are believed to be important to binding in the literature, the so-called *engineered features* [107]. For ligands, we construct the features using the counts of different atoms in the molecule (B, Br, C, Cl, F, I, P, N, O, S), total count of atoms, count of heavy atoms, rings, hydrogen donors, hydrogen acceptors, chiral centers, molecular weight and solubility. For proteins, we use the count of

² p -value (Benjamini Hochberg - False Discovery Rate corrected)

each amino acid, total number of amino acids, and sum of their overall molecular weight. In this set-up, ligands and proteins are represented using 18- and 22-dimensional features, respectively, instead of the original 300 dimensions for Mol2vec and 100 dimensions in ProtVec. Leveraging these engineered features, we observe inductive performance proximal to VecNet (Table S4).

We further explore which dimensions of Mol2vec and ProtVec are the best in explaining the engineered features. We do so by learning matrix E through algebraic decomposition, with $VE = F$, $V \in \mathbb{R}^{N_{ligands}, 300}$ for ligands, and $V \in \mathbb{R}^{N_{proteins}, 100}$ for proteins. Matrix F encodes the engineered features: for ligands we have $F \in \mathbb{R}^{N_{ligands}, 18}$, while for proteins $F \in \mathbb{R}^{N_{proteins}, 22}$ [108]. We re-scale Mol2vec and ProtVec embeddings, as well as the engineered features, between $[0, 1]$ and perform non-negative matrix factorization to obtain E . The rows of E explain the relevance of each Mol2vec or ProtVec dimension to the engineered features. While investigating the relation between engineered features and embeddings, we observed that 15 dimensions of the 300 for Mol2Vec showed the highest variance, suggesting that relevant information is embedded in a smaller dimensional space compared to the standard dimension used in the literature. Similarly, for ProtVec we found a subset of 16 dimensions (Figure S13). On the same note, concatenating the engineered features with Mol2vec and ProtVec does not change the inductive performance of VecNet (Table S4). This experiment suggests that the engineered features do not add any extra information to the binding prediction task, i.e the two representations are highly correlated.

We further investigated the engineered features to understand which of them contribute most to protein-ligand binding as they have an intuitive and straightforward interpretation. SHAP [109] values show that count of carbon atoms, hydrogen acceptor count, number of chirals, count of fluorine atoms and count of oxygen atoms are the top 5 properties of a ligand that determine its binding to a protein. Presence of amino acids like Glutamic acid, Tryptophan, Asparagine, Methionine, and Threonine in a protein target, presence of aromatic rings (helps in π -stacking), presence of R groups, and N or C terminus of the protein molecules, drive protein-ligand binding (see Tables S5 and S6).

VecNet with engineered features achieves similar inductive test score as the original version. Yet, the predictions from VecNet using engineered features $\{p_{ij}^{VecNet-Engineered}\}$ show poor negative correlation with ΔG binding affinities obtained from auto-docking simulations in the Results Section ($r_{Spearman} = -0.10$), compared to the original VecNet with Mol2vec and ProtVec embeddings ($r_{Spearman} = -0.51$). We also observe a significant reduction in F1-score, from 0.82 to 0.64 (see Results).

Overall, when representing protein and ligand molecules in 2D, we find that only a small

subset of the features drive protein-ligand binding and are able to explain intuitive properties of the molecules. Simple molecular descriptors like the presence of R groups in the amino acids, different atom counts, charge distribution in the ligand molecule represented by hydrogen acceptor, and donor counts have significant predictive power for protein-ligand binding. However, these features do not provide insight into the surface structure of the molecules or their rigidity. Indeed, presence of binding pockets on proteins and rotatability of bonds in ligand molecules significantly influence protein-ligand binding. Including these relevant aspects into the prediction task would reduce the number of false positives, often determined by the lack of 3D structures in the model. Adding 3D features of ligands and proteins (e.g., shape of the molecules, rotation of bonds in ligand, location of binding pockets etc.) will help AI-Bind to learn the detailed mechanism behind protein-ligand binding and make more accurate predictions.

Supplementary References

- [77] Geirhos, R. *et al.* Shortcut learning in deep neural networks. *Nature Machine Intelligence* **2**, 665–673 (2020). URL <https://doi.org/10.1038/s42256-020-00257-z>.
- [78] Huang, K. *et al.* DeepPurpose: a deep learning library for drug-target interaction prediction. *Bioinformatics* (2020). URL <https://doi.org/10.1093/bioinformatics/btaa1005>.
- [79] Liu, T., Lin, Y., Wen, X., Jorissen, R. N. & Gilson, M. K. BindingDB: a web-accessible database of experimentally determined protein-ligand binding affinities. *Nucleic Acids Research* **35**, D198–D201 (2007). URL <https://doi.org/10.1093/nar/gkl999>.
- [80] Alstott, J., Bullmore, E. & Plenz, D. powerlaw: A python package for analysis of heavy-tailed distributions **9**, e85777 (2014). URL <https://doi.org/10.1371/journal.pone.0085777>.
- [81] Ross, S. The multivariate normal distribution and copulas. 97–109 (Elsevier, 2013). URL <https://doi.org/10.1016/b978-0-12-415825-2.00006-1>.
- [82] Barabási, A.-L. *Network Science* (Cambridge University Press, 2016).
- [83] Wishart, D. S. *et al.* DrugBank: a knowledgebase for drugs, drug actions and drug targets. *Nucleic Acids Research* **36**, D901–D906 (2007). URL <https://doi.org/10.1093/nar/gkm958>. https://academic.oup.com/nar/article-pdf/36/suppl_1/D901/18782085/gkm958.pdf.

- [84] Tang, J. *et al.* Drug target commons: A community effort to build a consensus knowledge base for drug-target interactions. *Cell Chemical Biology* **25**, 224–229.e2 (2018). URL <https://doi.org/10.1016/j.chembiol.2017.11.009>.
- [85] Foodb database. www.foodb.ca.
- [86] Yannai, S. (ed.) *Dictionary of Food Compounds* (CRC Press, New York, NY, USA, 2012), 2nd edn.
- [87] Afendi, F. M. *et al.* KNApSACk family databases: Integrated metabolite–plant species databases for multifaceted plant research. *Plant and Cell Physiology* **53**, e1–e1 (2011). URL <https://doi.org/10.1093/pcp/pcr165>.
- [88] Weininger, D. SMILES, a chemical language and information system. 1. introduction to methodology and encoding rules. *Journal of Chemical Information and Modeling* **28**, 31–36 (1988). URL <https://doi.org/10.1021/ci00057a005>.
- [89] Prakash, B. A., Sridharan, A., Seshadri, M., Machiraju, S. & Faloutsos, C. EigenSpokes: Surprising patterns and scalable community chipping in large graphs. In *Advances in Knowledge Discovery and Data Mining*, 435–448 (Springer Berlin Heidelberg, 2010). URL https://doi.org/10.1007/978-3-642-13672-6_42.
- [90] Jaeger, S., Fulle, S. & Turk, S. Mol2vec: unsupervised machine learning approach with chemical intuition. *Journal of chemical information and modeling* **58**, 27–35 (2018).
- [91] Asgari, E. & Mofrad, M. R. K. Continuous distributed representation of biological sequences for deep proteomics and genomics. *PLOS ONE* **10**, e0141287 (2015). URL <https://doi.org/10.1371/journal.pone.0141287>.
- [92] Mikolov, T., Chen, K., Corrado, G. & Dean, J. Efficient estimation of word representations in vector space. *arXiv preprint arXiv:1301.3781* (2013).
- [93] Rogers, D. & Hahn, M. Extended-connectivity fingerprints. *Journal of chemical information and modeling* **50**, 742–754 (2010).
- [94] Kingma, D. P. & Welling, M. Auto-encoding variational bayes. *arXiv preprint arXiv:1312.6114* (2013).
- [95] Jaeger, S., Fulle, S. & Turk, S. Mol2vec: Unsupervised machine learning approach with chemical intuition. *Journal of Chemical Information and Modeling* **58**, 27–35 (2018). URL <https://doi.org/10.1021/acs.jcim.7b00616>.

- [96] Mikolov, T., Sutskever, I., Chen, K., Corrado, G. S. & Dean, J. Distributed representations of words and phrases and their compositionality. In *Advances in neural information processing systems*, 3111–3119 (2013).
- [97] Rogers, D. & Hahn, M. Extended-connectivity fingerprints. *Journal of Chemical Information and Modeling* **50**, 742–754 (2010). URL <https://doi.org/10.1021/ci100050t>.
- [98] Koch, G., Zemel, R. & Salakhutdinov, R. Siamese neural networks for one-shot image recognition. In *ICML deep learning workshop*, vol. 2 (Lille, 2015).
- [99] Doersch, C. Tutorial on variational autoencoders. *arXiv preprint arXiv:1606.05908* (2016). URL <https://arxiv.org/abs/1606.05908>.
- [100] Kingma, D. P., Salimans, T. & Welling, M. Variational dropout and the local reparameterization trick. In Cortes, C., Lawrence, N. D., Lee, D. D., Sugiyama, M. & Garnett, R. (eds.) *Advances in Neural Information Processing Systems 28*, 2575–2583 (Curran Associates, Inc., 2015). URL <http://papers.nips.cc/paper/5666-variational-dropout-and-the-local-reparameterization-trick.pdf>.
- [101] Newcombe, R. G. Two-sided confidence intervals for the single proportion: comparison of seven methods **17**, 857–872 (1998). URL [https://doi.org/10.1002/\(sici\)1097-0258\(19980430\)17:8<857::aid-sim777>3.0.co;2-e](https://doi.org/10.1002/(sici)1097-0258(19980430)17:8<857::aid-sim777>3.0.co;2-e).
- [102] Papadopoulos, J. S. & Agarwala, R. COBALT: constraint-based alignment tool for multiple protein sequences. *Bioinformatics* **23**, 1073–1079 (2007). URL <https://doi.org/10.1093/bioinformatics/btm076>.
- [103] Edgar, R. C. MUSCLE: multiple sequence alignment with high accuracy and high throughput. *Nucleic Acids Research* **32**, 1792–1797 (2004). URL <https://doi.org/10.1093/nar/gkh340>.
- [104] Yu, G. Using ggtree to visualize data on tree-like structures. *Current Protocols in Bioinformatics* **69** (2020). URL <https://doi.org/10.1002/cpbi.96>.
- [105] Wang, L.-G. *et al.* Treeio: An r package for phylogenetic tree input and output with richly annotated and associated data. *Molecular Biology and Evolution* **37**, 599–603 (2019). URL <https://doi.org/10.1093/molbev/msz240>.
- [106] Asgari, E. & Mofrad, M. R. Continuous distributed representation of biological sequences for deep proteomics and genomics. *PloS one* **10**, e0141287 (2015).

- [107] Rohrer, S. G. & Baumann, K. Maximum unbiased validation (MUV) data sets for virtual screening based on PubChem bioactivity data. *Journal of Chemical Information and Modeling* **49**, 169–184 (2009). URL <https://doi.org/10.1021/ci8002649>.
- [108] Henderson, K. *et al.* Rolx: structural role extraction & mining in large graphs. In *Proceedings of the 18th ACM SIGKDD international conference on Knowledge discovery and data mining*, 1231–1239 (2012).
- [109] Lundberg, S. M. & Lee, S.-I. A unified approach to interpreting model predictions. In Guyon, I. *et al.* (eds.) *Advances in Neural Information Processing Systems 30*, 4765–4774 (Curran Associates, Inc., 2017).

Table SI. 1: Transductive performance of a duplex configuration model on unipartite layers with varying $P(k)$ annotation distribution and $r_{Spearman}(k, \langle K_d \rangle)$. The constrained features are consistent with the protein sample in BindingDB. The kinetic constant of a link is chosen as the geometric mean of the sampled K_d values associated with its end nodes.

Annotation distribution	Correlation	AUROC	AUPRC
Power-law	$r_{Spearman}(k, \langle K_d \rangle) \approx -0.47$	0.84	0.61
Power-law	$r_{Spearman}(k, \langle K_d \rangle) \approx 0$	0.78	0.39
Poisson	$r_{Spearman}(k, \langle K_d \rangle) \approx -0.47$	0.71	0.32
Poisson	$r_{Spearman}(k, \langle K_d \rangle) \approx 0$	0.54	0.19

Table SI. 2: As path length to a fixed protein i increases, the mean and variance of the length of the low-dimensional embedding of the ligand $\|\bar{u}_j\|$ decrease.

Path Length i to j	1	3	5	7	9	11	13
Mean $\ \bar{u}_j\ $	0.045	0.035	0.014	0.004	0.001	0.0001	$5 \cdot 10^{-7}$
Std. dev. $\ \bar{u}_j\ $	0.075	0.035	0.025	0.014	0.008	0.001	$4 \cdot 10^{-6}$

Table SI. 3: **Results across different models.** We summarize all performances on the network-derived negative samples. We perform 5-fold cross-validation, reporting AUROC and AUPRC averaged over the 5 runs with random initialization and data split. Results are reported separately on 3 different train-validation-test splits with different data held out in the validation and testing sets: (1) **Edges (Transductive test)** - test sets contain unseen edges in the train network, (2) **Targets (Semi-inductive test)** - test sets contains pairs with proteins that do not appear in train or validation set, (3) **Nodes (Inductive test)** - nodes in test set pairs are completely disjoint from train set. *Random Input Tests:* We train and test AI-Bind’s VecNet replacing node features with random entries drawn from a uniform distribution in the range $U([-1, 1]^d)$. We run two tests (1) Unif. - All node features are replaced by vectors drawn from a uniform distribution $U([-1, 1]^d)$, (2) Unif.Targ. - Only the target node features are replaced by vectors from $U([-1, 1]^d)$; drug features remaining the same. Note that the transductive (unseen edges) performance is reported based on the models optimized for unseen nodes, except for the case of the Random Inputs, where we report performance based on models optimized for unseen targets.

Model	Test Data Division					
	Edges		Targets		Nodes	
	AUROC	AUPRC	AUROC	AUPRC	AUROC	AUPRC
Configuration	.738 ± .014	.739 ± .017	.754 ± .021	.691 ± .038	.500 ± .000	.469 ± .014
VecNet	.794 ± .008	.817 ± .013	.779 ± .025	.752 ± .039	.745 ± .032	.729 ± .038
Siamese	.664 ± .027	.637 ± .003	.666 ± .031	.621 ± .032	.639 ± .026	.583 ± .025
VAENet	.777 ± .010	.701 ± .048	.756 ± .022	.710 ± .030	.740 ± .024	.701 ± .048
DeepPurpose	.775 ± .025	.800 ± .025	.642 ± .022	.591 ± .042	.642 ± .025	.583 ± .016
<i>Random Inputs</i>						
VecNet Unif.	.668 ± .012	.702 ± .015	.539 ± .019	.541 ± .013	.466 ± .054	.456 ± .041
VecNet - Targ.	.704 ± .008	.725 ± .009	.575 ± .032	.556 ± .025	.558 ± .009	.501 ± .021

Table SI. 4: **Optimal feature selection:** We observe that AI-Bind’s VecNet shows similar performances in inductive tests, when Mol2vec and ProtVec are replaced by simple engineered features encoding certain properties of protein and ligand molecules. Furthermore, we observe that only 15 dimensions of Mol2vec and 16 dimensions of ProtVec embeddings encode these molecular properties driving the binding task. Using these feature subsets of Mol2vec and ProtVec helps VecNet achieving similar inductive performance. Concatenating the engineered features with Mol2vec and ProtVec does not improve inductive performance. This suggests that the information encoded in the engineered features strongly correlates with Mol2vec and ProtVec embeddings.

Performance	Original	Engineered features	Mol2vec and ProtVec dimensions explaining Engineered Features	Concatenated: Mol2vec/ProtVec + Engineered features
AUROC	0.75 ± 0.032	0.73 ± 0.032	0.72 ± 0.066	0.75 ± 0.033
AUPRC	0.73 ± 0.038	0.74 ± 0.033	0.72 ± 0.057	0.73 ± 0.042

Table SI. 5: **Engineered feature importance for ligands:** We tabulate the engineered features in descending order of average absolute SHAP importance over AI-Bind data. A higher SHAP value represents more relevance of the molecular property in predicting protein-ligand binding.

Feature	Average SHAP Importance
Count of Carbon Atom	0.012546
Hydrogen Acceptor Count	0.012362
Number of Chirals	0.008750
Count of Flourine Atoms	0.006527
Count of Oxygen Atoms	0.006184
Hydrogen Donor Count	0.005647
Number of Atoms	0.004165
Count of Heavy Atoms	0.003468
Solubility in Water ($\log p$)	0.003202
Molecular Weight	0.003161
Count of Nitrogen Atoms	0.002007
Count of Chlorine Atoms	0.001720
Count of Sulphur Atoms	0.001483
Number of Rings	0.000525
Count of Phosphorus Atoms	0.000191
Count of Iodine Atoms	0.000130
Count of Bromine Atoms	0.000083
Count of Boron Atoms	0.000070

Table SI. 6: **Engineered feature importance for proteins:** We tabulate the engineered features in descending order of average absolute SHAP importance over AI-Bind data. A higher SHAP value represents more relevance of the molecular property in predicting protein-ligand binding.

Feature	Average SHAP Importance
Count of Glutamic acid (E)	0.036747
Count of Tryptophan (W)	0.033210
Count of Asparagine (N)	0.024770
Count of Methionine (M)	0.022734
Count of Threonine (T)	0.021194
Count of Glycine (G)	0.020832
Count of Arginine (R)	0.019599
Count of Phenylalanine (F)	0.017040
Count of Cysteine (C)	0.016428
Count of Isoleucine (I)	0.016215
Count of Alanine (A)	0.015732
Count of Histidine (H)	0.014813
Count of Leucine (L)	0.014026
Count of Tyrosine (Y)	0.013844
Count of Proline (P)	0.013014
Count of Valine (V)	0.011152
Count of Serine (S)	0.010930
Count of Lysine (K)	0.008689
Count of Aspartic acid (D)	0.008303
Total amino acid count	0.003381
Count of Glutamine (Q)	0.002957
Molecular Weight	0.002088

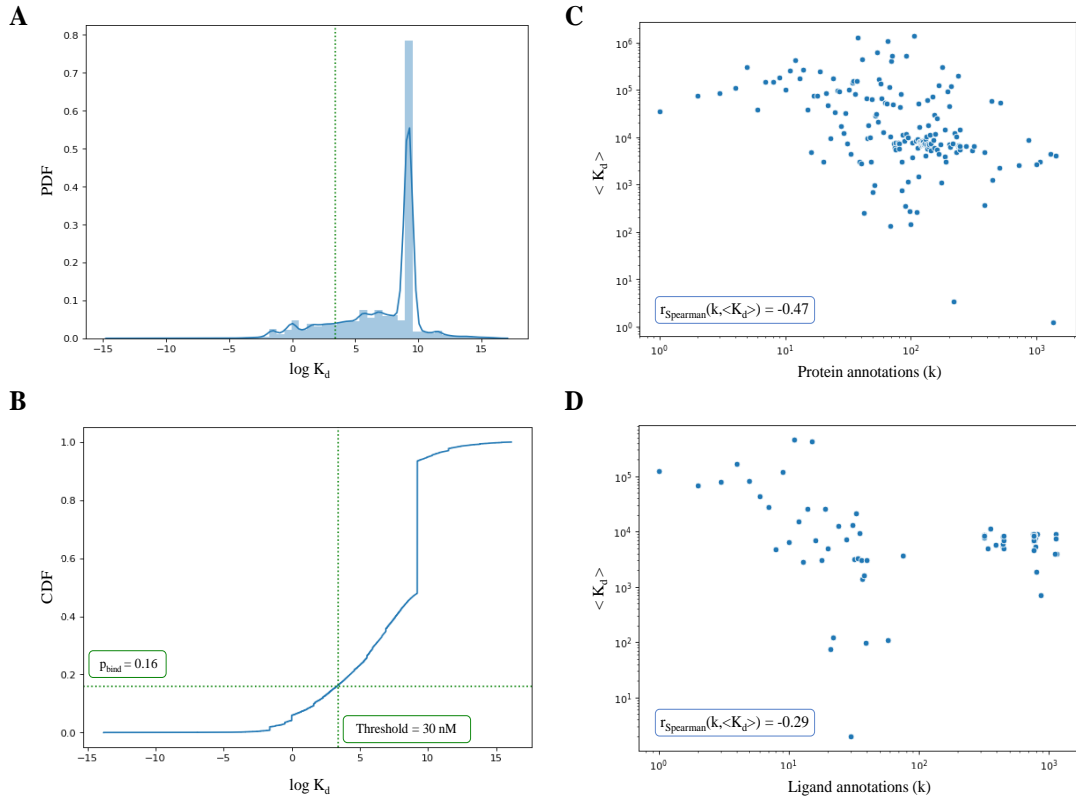


Figure SI. 1: **Disassociation constant K_d and its relation with the number of annotations/records per node k in BindingDB.** (A)-(B) Density distribution and cumulative distribution of $\log(K_d)$. With threshold 30 nM , we obtain an average binding probability $p_{bind} = 0.16$. (C)-(D) Each node is characterized by the number of annotations k , and the average $\langle K_d \rangle$ over its records. We find that k and $\langle K_d \rangle$ are anti-correlated. This implies that proteins and ligands with higher number of annotations tend to have lower K_d on average, i.e., stronger binding.

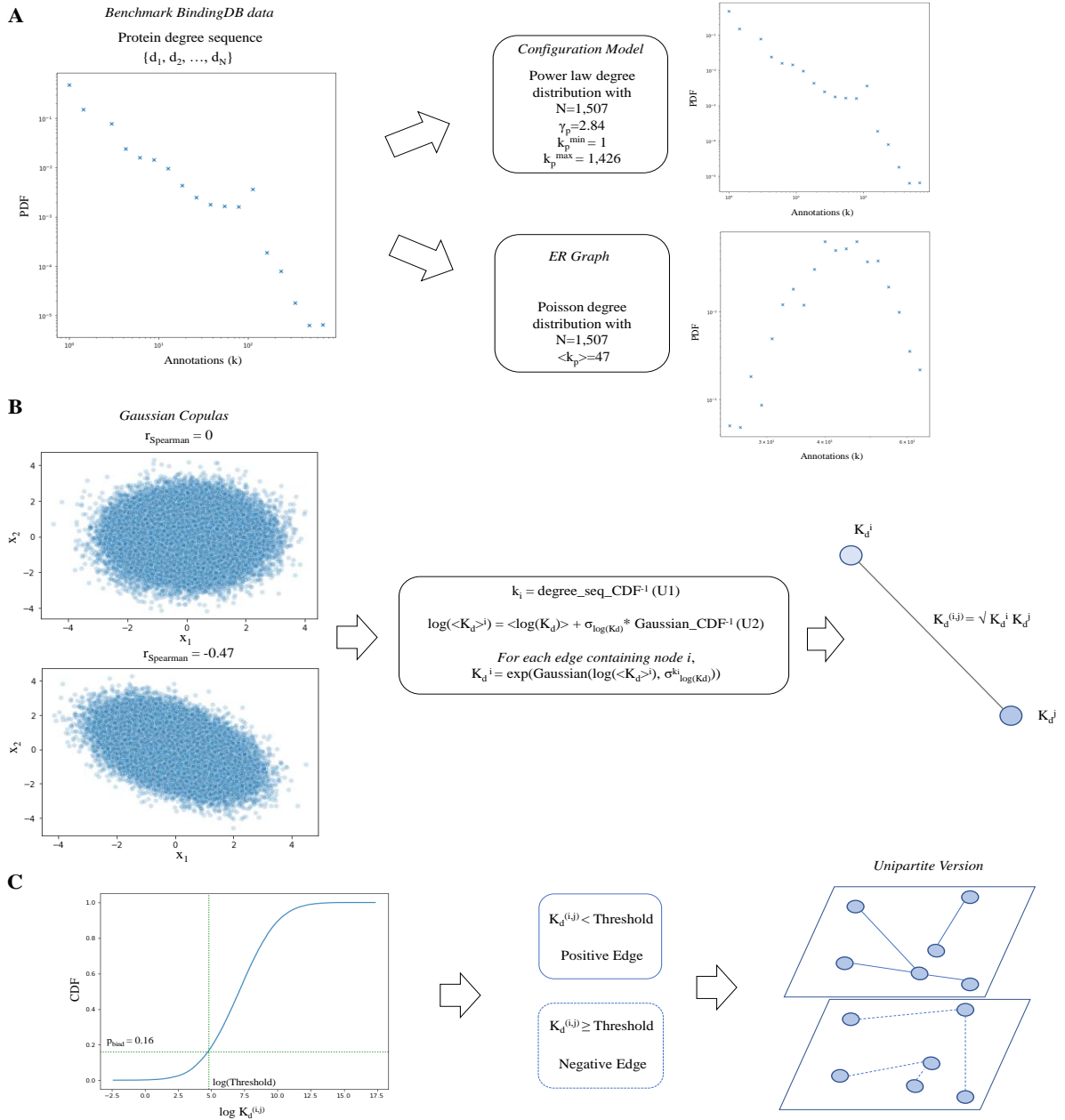


Figure SI. 2: **Experimental set-up for studying the emergence of topological short-cuts.** **(A)** We generate random unipartite networks inspired by the topological and kinetic features of the protein sample in BindingDB. In particular, we fix the size of the network to $N = 1,507$, and generate power-law distributions compatible with the fitted $\gamma = 2.84$, while for the Poisson case the link density is constrained by the average number of annotations per protein $\langle k \rangle = 47$. **(B)** We generate uncorrelated and anti-correlated Gaussian copulas for the variables x_1 and x_2 . U_1 and U_2 are their marginal CDFs of the joint probability distribution representing a 2-D Gaussian with the desired level of correlation. The inverse cumulative distribution $degree_seq_CDF^{-1}$ is used to sample the set of annotations $\{k_i\}$, where $degree_seq_CDF^{-1}$ is different for power law and Poisson distributions. After drawing for any node i the average kinetic constant per link $\langle K_d \rangle^i$, depending on the degree k_i of a selected node we further draw k_i kinetic constants from a log-normal distribution with logarithmic parameters $\log(\langle K_d \rangle^i)$ and $\sigma_{\log(K_d)}^{k_i}$, i.e the expected standard deviation of the kinetic constants across the links for all nodes with degree equal to k_i in the original data. The final disassociation constant $K_d^{(i,j)}$ assigned to edge (i, j) is the geometric average of the contribution K_d^i from node i and the contribution K_d^j from node j . **(C)** We select as threshold for $K_d^{(i,j)}$ the value for which 16% of the annotations become positive or binding, enforcing the constraint on the observed p_{bind} . Based on this threshold, we generate the duplex layers with positive and negative edges and calculate the multilink degree sequences, input to the configuration model (see Methods in the main text).

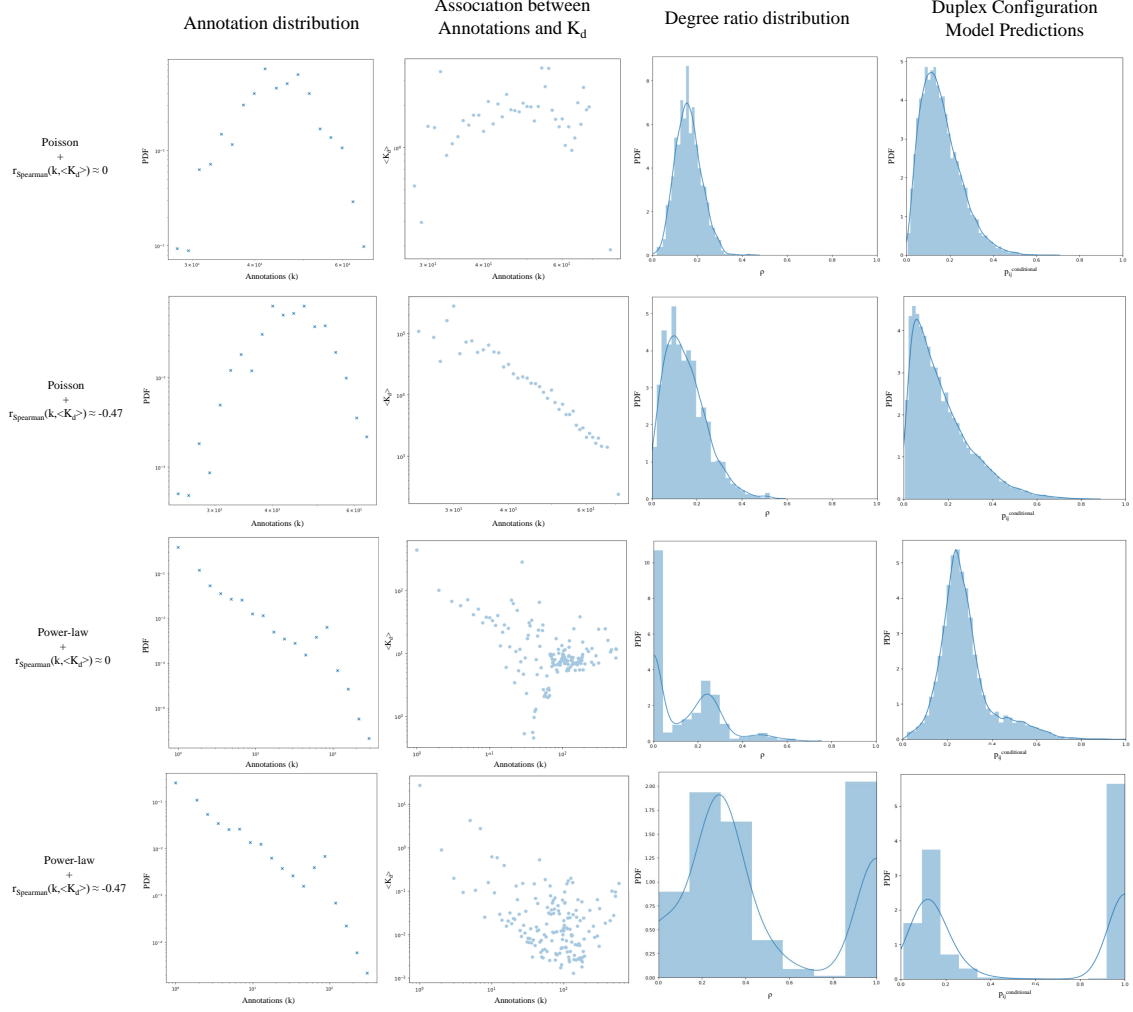


Figure SI. 3: **Emergence of annotation imbalance.** We observe different degrees of annotation imbalance, as quantified by the varying extent of variability characterizing the degree ratio ρ (Eq. 1 in the main text). Different combinations of $P(k)$ and $c_{Spearman}(k, \langle K_d \rangle)$ influence the behavior of ρ , in turn, constraining the configuration model prediction $\{p_{ij}^{conditional}\}$. Only when annotations are distributed according to a power law, and k and $\langle K_d \rangle$ are not independent, we observe annotation imbalance emerging.

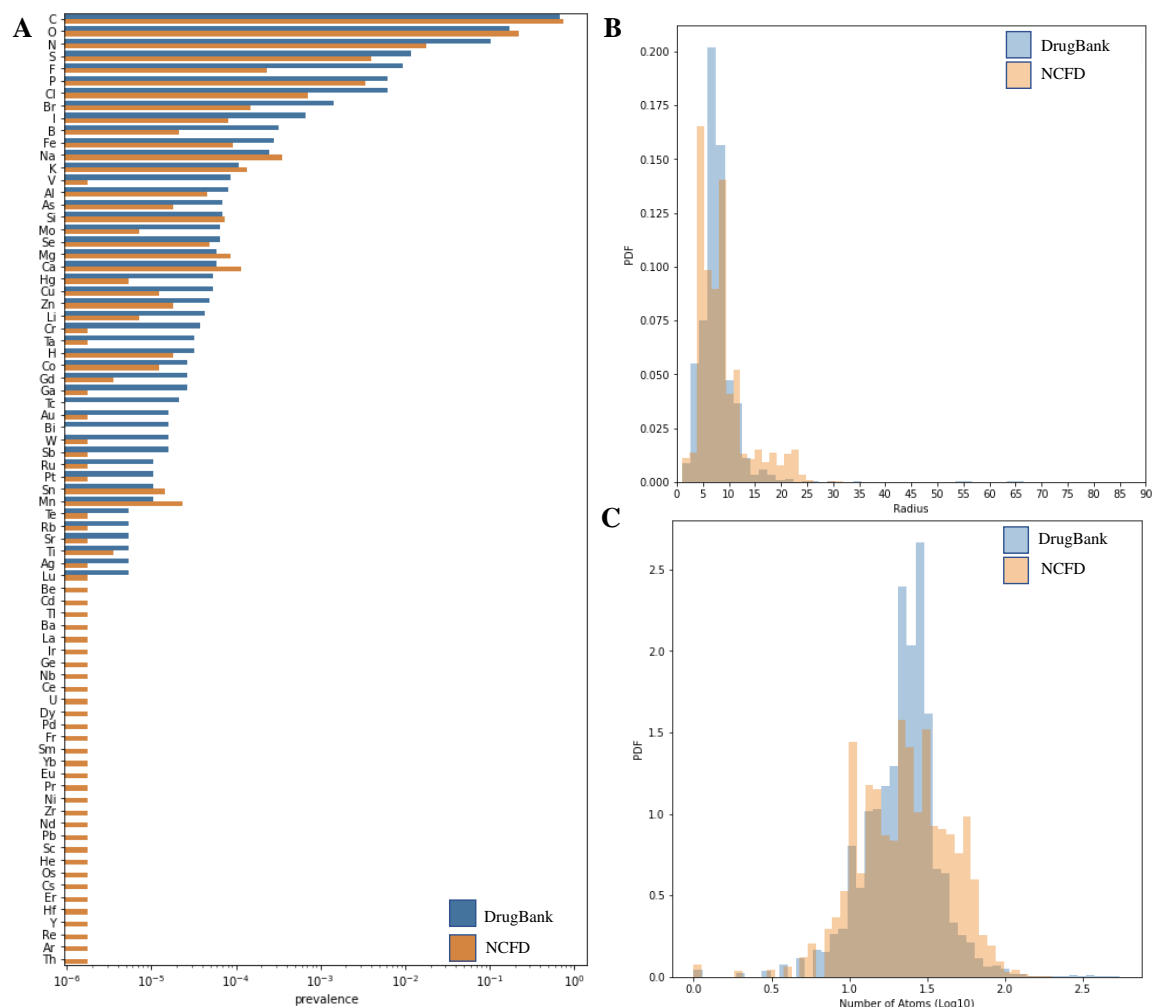


Figure SI. 4: **Naturally occurring compounds are structurally more complex than drugs.** (A) Prevalence of different atoms in DrugBank and natural ligands present in NCFD. Natural ligands show more diversity in terms of the constituent atoms. (B) The distribution of the radius across the ligand molecules in DrugBank and NCFD, and (C) The distribution of the number of atoms across the ligand molecules in DrugBank and NCFD.

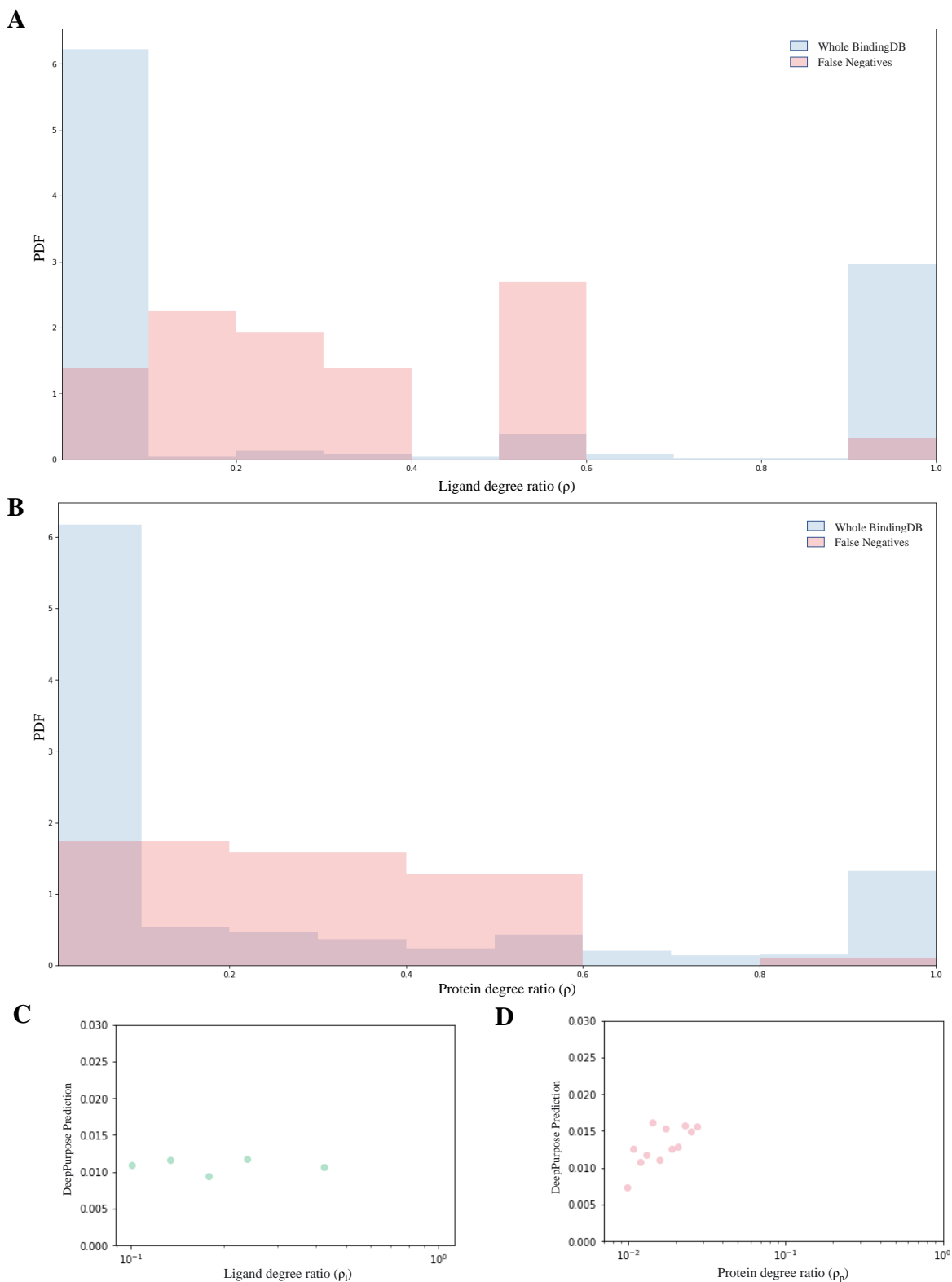


Figure SI. 5: **Annotation bias in top 100 false negative predictions made by DeepPurpose.** (A)-(B) Degree ratio distribution of the nodes involved in the false negative predictions is shown compared to all the nodes in the BindingDB data. The false negative predictions correspond to proteins and ligands with low degree ratios. (C)-(D) DeepPurpose predicts lower binding probabilities for the nodes with lower degree ratios.

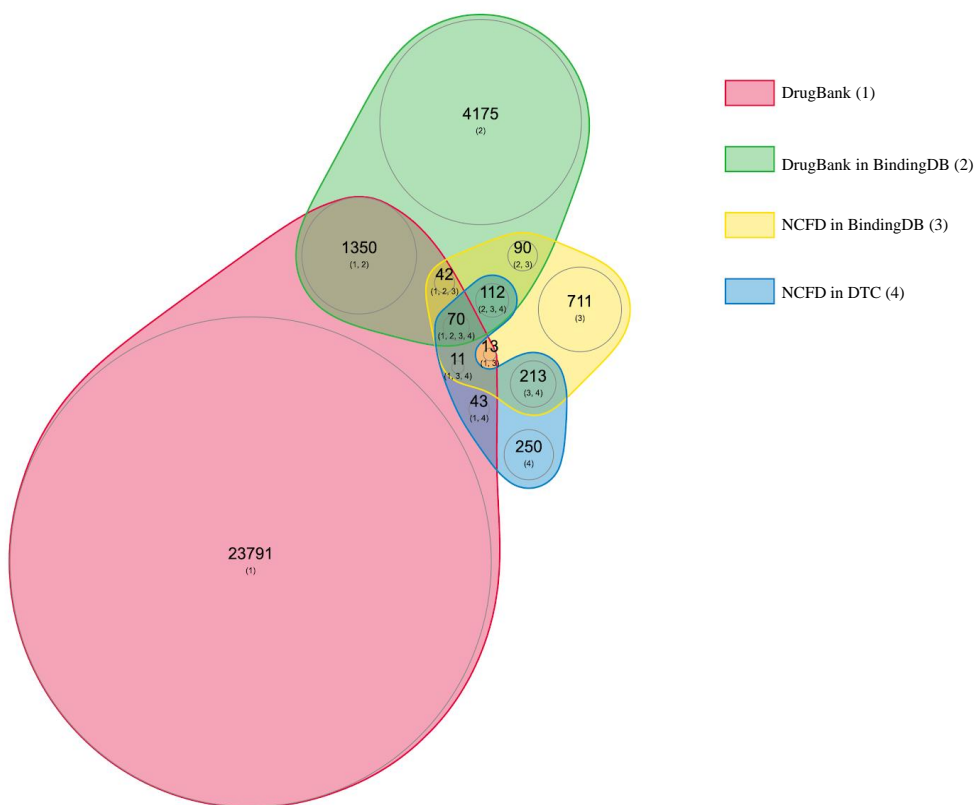


Figure SI. 6: **Venn diagram of positive binding samples across different databases.** AI-Bind training data combines protein-ligand binding data from three databases: DrugBank, BindingDB, and Drug Target Commons (DTC). Majority of the binding examples are taken from DrugBank. BindingDB and DTC are used to obtain additional protein-ligand pairs, especially to maximize the binding information involving naturally occurring ligands.

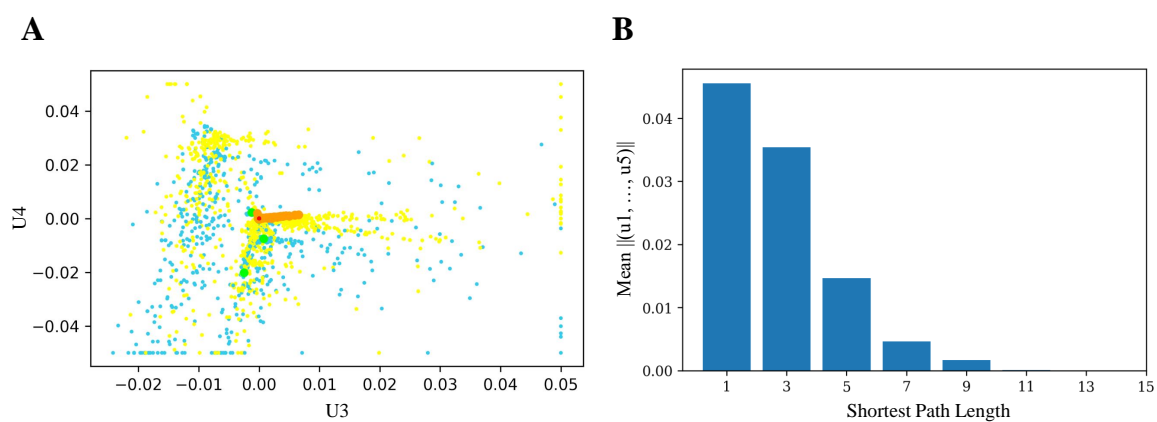


Figure SI. 7: **EigenSpokes Analysis.** (A) Network-based dimension reduction of nodes in the full protein-ligand network. Node i is represented by the vector $\bar{u}_i = (u_1, u_2, u_3, u_4, u_5) \in \mathbb{R}^5$. Here we visualize (u_3, u_4) for only the ligands. Coloring is based on the hop-distances from an example target BPT4: Green = 1 hop, Blue = 3 hops, Yellow = 5 hops, Orange = 7 hops, Red ≥ 9 hops. We see that at > 7 hop, most nodes are very close to the origin. (B) Mean of all reduced vector magnitudes $\|\bar{u}_j\|$ averaged over all pairs (i, j) of a given path length. We see a significant decrease in magnitude as the shortest path length increases.

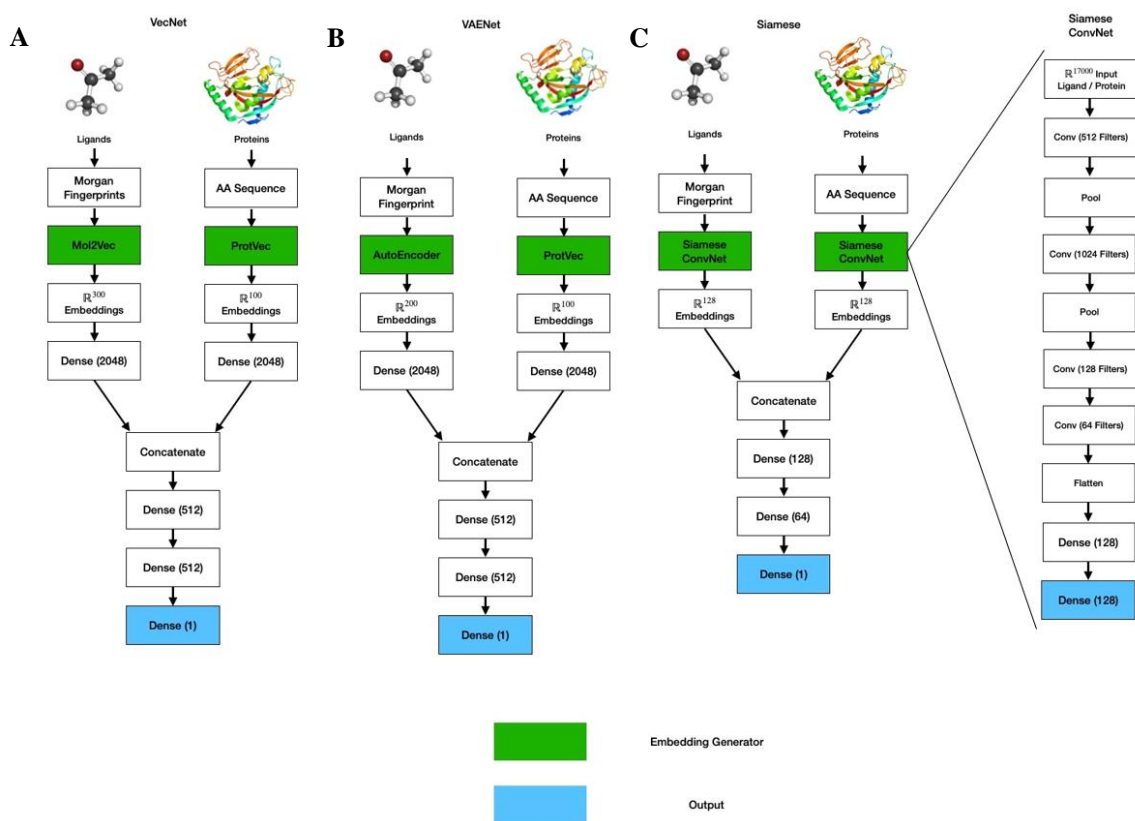


Figure SI. 8: **Deep architectures of VecNet, VAENet, and Siamese model.** (A) VecNet uses Mol2vec and ProtVec as the unsupervised pre-trained models for ligand and protein embeddings respectively. The dense layers act as decoders, and are trained using the network-derived dataset. (B) VAENet architecture is similar to VecNet, where Mol2vec embeddings are replaced with embeddings obtained from a variational auto-encoder. This auto-encoder is trained on ≈ 9.5 million compounds from the ZINC database. (C) Siamese model embeds both proteins and ligands onto the same latent space. Siamese ConvNet blocks minimize the triplet loss between the proteins binding to the same ligand. We follow a similar approach for generating the ligand embeddings.

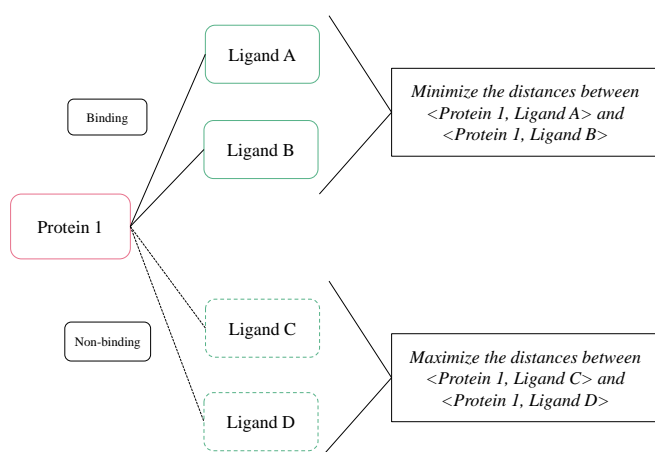
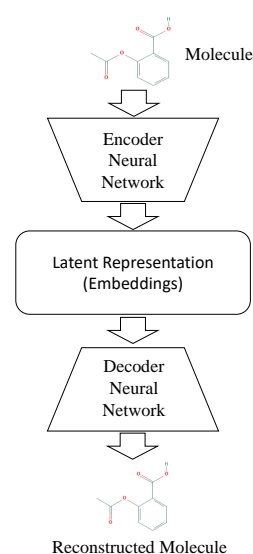
A**B**

Figure SI. 9: **Logical flow of the Siamese Model and Variational Auto-Encoder.** (A) We minimize the embedded Euclidean distances between the proteins which bind to the same ligand, and maximize the distance between the non-binding ones. Similar logic is applied for creating the ligand embeddings. (B) Variational auto-encoder minimizes the reconstruction loss for the ligands to create a latent space embeddings. We generate Morgan fingerprints from the isomeric SMILES and feed that to the auto-encoder. The auto-encoder generates latent space representations by minimizing reconstruction loss on the fingerprints.

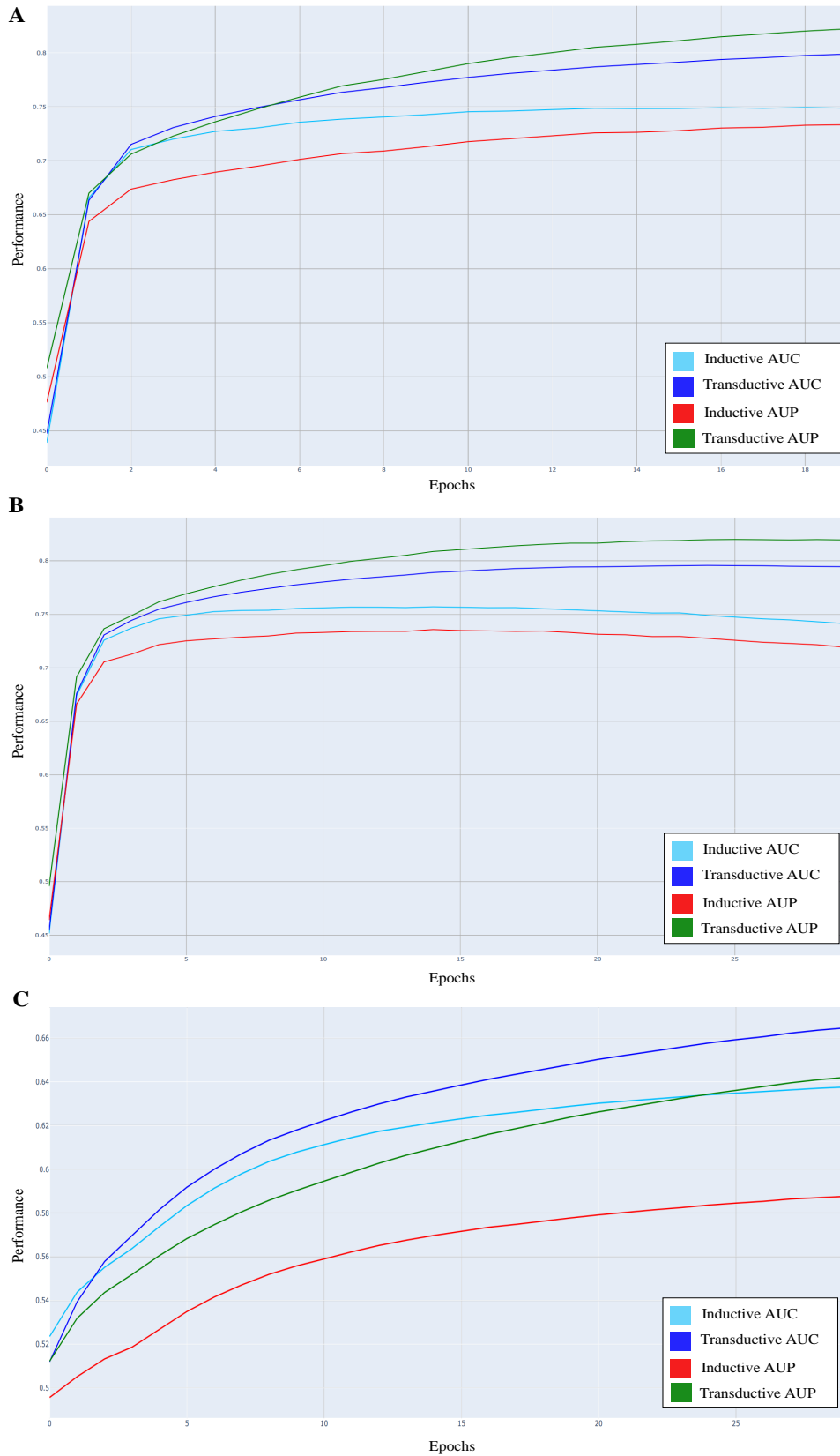


Figure SI. 10: **Training curves for three AI-Bind architectures.** We plot the training curves for **(A)** VecNet, **(B)** VAENet, and **(C)** Siamese model over 30 epochs. The AUROC and the AUPRC are separately shown for the transductive (unseen edges) and inductive (unseen nodes) test scenarios.

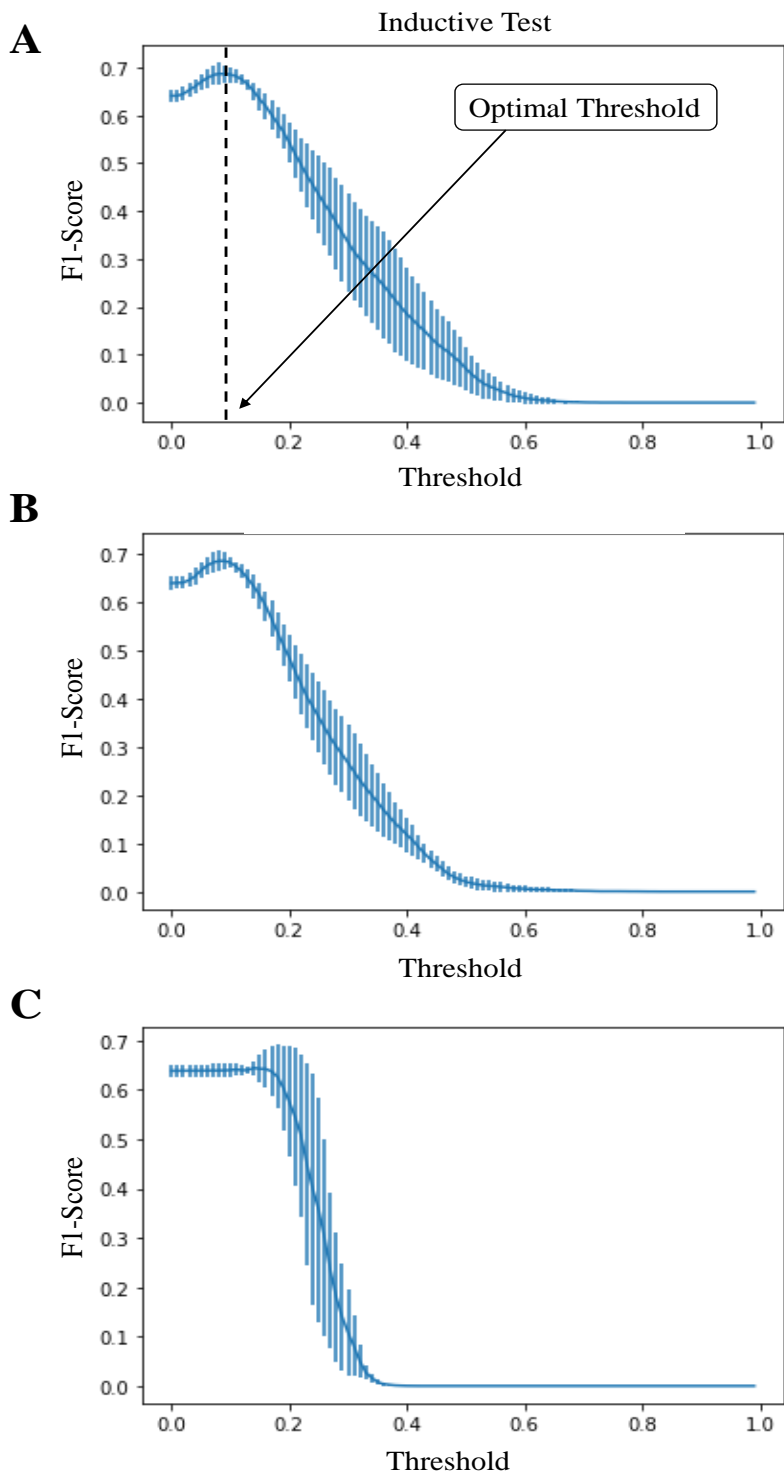


Figure SI. 11: **F1-Score and Optimal Threshold.** We plot the F1-scores for the trained (A) VecNet, (B) VAENet, and (C) Siamese models relative to the classification threshold in the inductive test scenario. The threshold value corresponding to the highest F1-score is considered as the optimal threshold, and is used to obtain the binary labels from the predicted binding probabilities. For VecNet, we obtain an optimal threshold of 0.09.

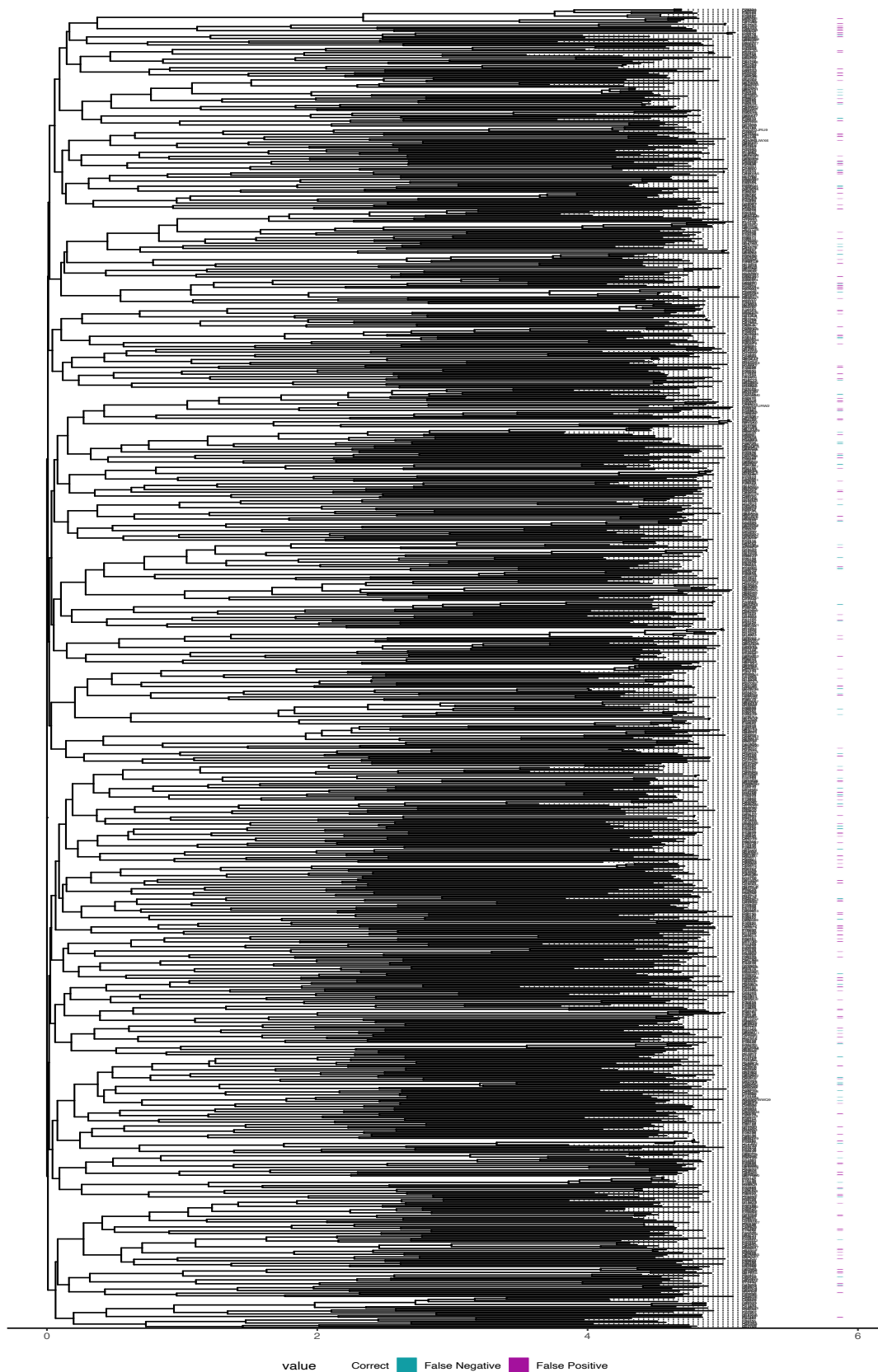


Figure SI. 12: **Phylogenetic tree of genes enriched towards prediction bias.** We compare proteins associated with the false predictions (both false positives and false negatives) made by AI-Bind’s VecNet to uncover structural similarities. AI-Bind does not show any bias towards certain protein structures in the false predictions, and can be used for binding prediction involving protein structures emerging from different organisms.

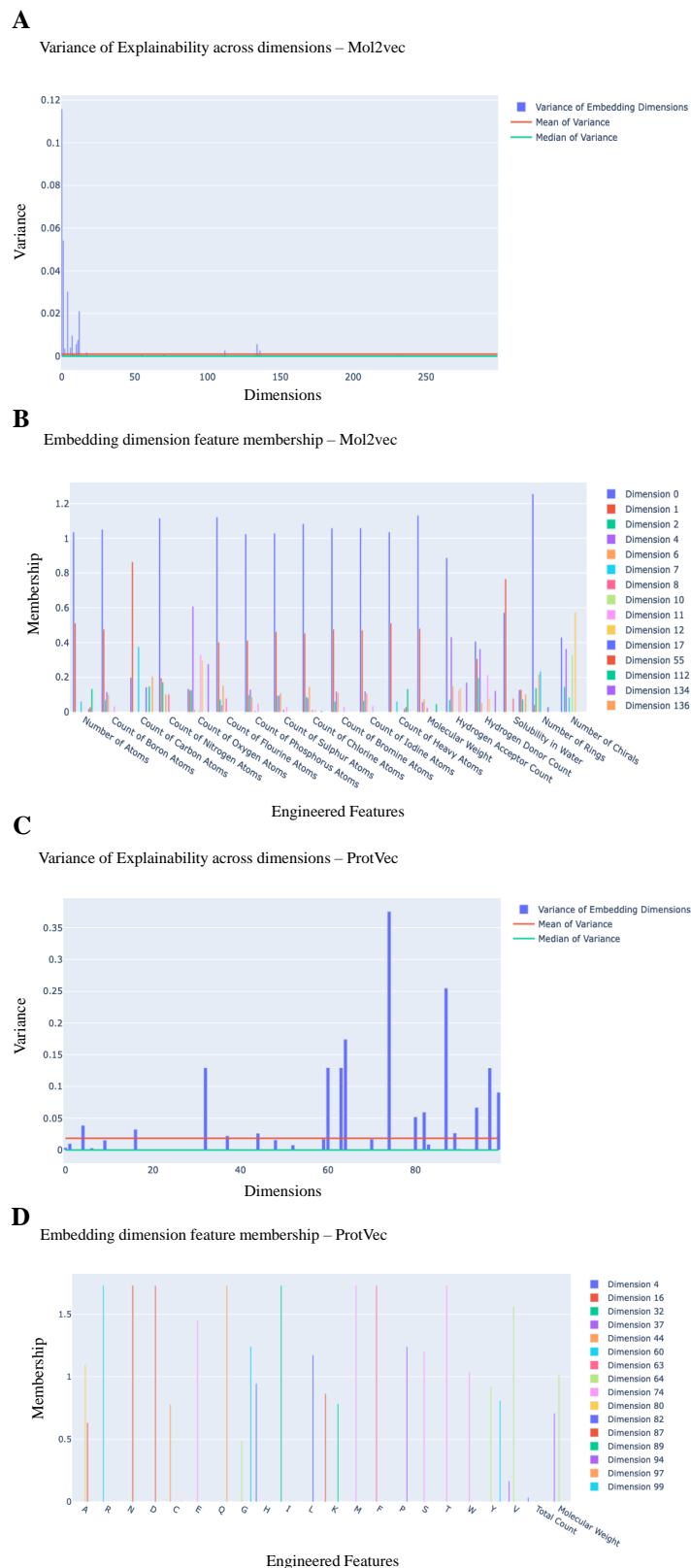


Figure SI. 13: **Dimensions of Mol2vec and ProtVec contributing to protein-ligand binding.** (A)-(B) Only 15 Mol2vec dimensions show high variability when explaining the engineered features representing ligand molecules. (C)-(D) We find similar results for 16 ProtVec dimensions.